

# **Novel Bioresorbable Hematene-Doped Monetite Scaffold for Bone Repair**

By

**Rachel Monk**

Department of Surgery

Division of Experimental Surgery

McGill University, Montréal

December 2022



A thesis submitted to McGill University in partial fulfillment of the requirements of the degree  
of Master of Science

© Rachel Monk 2022

## TABLE OF CONTENTS

ABSTRACT.....	III
RÉSUMÉ .....	IV
ACKNOWLEDGEMENTS .....	V
CONTRIBUTION OF AUTHORS .....	V
LIST OF ABBREVIATIONS.....	VI
LIST OF TABLES .....	VII
LIST OF FIGURES.....	VII
THESIS INTRODUCTION.....	1
<b>CHAPTER 1: BONE GRAFTING AND BONE SUBSTITUTES .....</b>	<b>2</b>
1.1 BONE GRAFTING .....	2
1.2 BONE TISSUE ENGINEERING .....	3
1.2.1 Tissue engineered scaffolds.....	5
1.2.2 Scaffold requirements.....	6
I) Biological .....	6
II) Mechanical .....	7
III) Structural.....	8
1.3 SYNTHETIC BONE GRAFT SUBSTITUTES.....	9
1.3.1 Calcium phosphate-based bioceramics .....	9
I) Hydroxyapatite.....	10
II) Brushite and Monetite .....	10
<b>CHAPTER 2: NANOMATERIALS IN BONE TISSUE ENGINEERING .....</b>	<b>11</b>
2.1 INTRODUCTION .....	11
2.2 METAL NANOSTRUCTURED PARTICLES .....	12
2.3 TWO-DIMENSIONAL NANOMATERIALS .....	14
2.3.1 Graphene-family nanomaterials .....	14
I) Graphene .....	14
II) Graphene oxide (GO) .....	15
III) Reduced graphene oxide (rGO).....	16
2.3.1.1 Toxicity of graphene-family nanomaterials .....	17
2.3.2 Novel 2D Hematene .....	17
2.4 NANO-DOPED CALCIUM PHOSPHATE CEMENTS.....	18
<b>CHAPTER 3: HEMATENE-DOPED MONETITE SCAFFOLD FOR BONE REPAIR .....</b>	<b>20</b>
3.1 RATIONALE.....	20
3.2 HYPOTHESIS .....	21
3.3 STUDY OBJECTIVES .....	21
3.4 EXPERIMENTAL SECTION.....	22
3.4.1 Materials.....	22
3.4.2 Characterizations.....	23
3.4.3 Absorption, decomposition, and mechanical testing .....	24
3.4.4 In vitro testing.....	25
3.4.5 Statistical analysis.....	26
<b>CHAPTER 4: RESULTS .....</b>	<b>27</b>
4.1 CHARACTERIZATIONS .....	27
4.1.2 Transmission electron microscopy (TEM) .....	27
4.1.3 X-ray diffraction (XRD) .....	28
4.1.4 Scanning electron microscope (SEM).....	28

4.1.5 Thermogravimetric analysis (TGA).....	29
4.1.6 Micro-computed tomography (micro-CT).....	30
4.1.7 Degradation behaviour.....	31
4.1.8 Compressive strength .....	32
4.2 IN VITRO FINDINGS .....	33
4.2.1 Cell proliferation .....	33
4.2.2 Cell viability .....	33
4.2.3 Cell adhesion .....	35
4.2.4 Alkaline phosphatase (ALP) activity.....	35
4.2.5 Real-time quantitative reverse transcription (RT-qPCR).....	36
<b>CHAPTER 5: DISCUSSION AND CONCLUSION.....</b>	<b>38</b>
5.1 DISCUSSION.....	38
5.2 CONCLUSION.....	42
5.3 FUTURE WORKS .....	42
<b>References.....</b>	<b>43</b>
<b>Appendices.....</b>	<b>54</b>

## ABSTRACT

Autografts remain the gold standard for the repair of bone defects despite their limited supply, donor-site morbidity, and associated increased surgical times. Synthetic materials with osteoconductive or osteoinductive abilities have developed as alternative avenues with considerable focus surrounding the construction of three-dimensional scaffolds. Dicalcium phosphates are one favorable option due to their compositional resemblance to native bone, metastability in physiological fluids, and advanced resorptive profiles. Recent developments with nanomaterial lattices have allowed scaffold systems, especially calcium phosphates, to optimize their mechanical and biological performances. Graphene, a 2D atomic layer of carbon is an example of a well-publicized material that has improved the strength, functionality, and osteogenic potency of a variety of scaffolds with its dimensional properties. Excitingly, hematene as a novel ultrathin 2D nanosheet of iron oxide has been customized in our laboratory to introduce an unconventional route to 2D material discovery with 3D bonding networks. In this work, we display the simplicity of obtaining ultrathin hematene nanosheets through ultrasonic exfoliation and their decoration over monetite implants to facilitate bone repair. Hematene-loaded scaffolds displayed improved mechanical performances with good thermal stability and degradation profiles. Scaffolds were biocompatible and supported MC3T3-E1 cell infiltration, adhesion, and increased proliferation. Furthermore, hematene loading significantly improved the osteogenic potency of monetite scaffolds with enhanced bone biomarker profiles with osteoinductive agents. This work uncovers the therapeutic potential of hematene derivatives for the first time and specifically highlights their further potential as the next interesting scaffold candidate for bone tissue regeneration.

## RÉSUMÉ

Les autogreffes continuent d'être le standard pour la réparation des défauts osseux malgré leurs limitations avec les risques de morbidités au site donneur et les augmentations des durées de chirurgies. Les matériaux synthétiques avec des capacités ostéoconducteurs ou ostéoinductifs ont été développés comme des voies alternatives avec une attention considérable autour de la construction d'implant en trois dimensions. Les phosphates de dicalciums sont des options très favorable en raison de leurs ressemblances à la composition de l'os natif, de leur métastabilité dans les fluides physiologiques et de leurs capacités de résorption avancés. Les développements récents avec des réseaux de nanomatériaux ont permis aux systèmes d'implants, en particulier ceux en phosphate de calcium, d'optimiser leurs performances mécaniques et biologiques. Le graphène, une couche atomique 2D de carbone, est un exemple de matériel bien connu qui a amélioré la résistance, la fonctionnalité et la puissance ostéogénique d'une variété d'implants grâce à ses propriétés dimensionnelles. De manière excitante, le Hématène, une nouvelle feuille nano en 2D et ultra-mince d'oxyde de fer a été développée dans notre laboratoire et a introduit une voie non conventionnelle vers la découverte de matériaux 2D avec ses réseaux de liaison 3D. Dans ce travail, nous avons montré la simplicité d'obtention des feuilles nano d'hématène ultra-minces par l'exfoliation ultrasonique et leurs décorations sur des implants en monétite pour faciliter la réparation osseuse. Les implants chargés d'hématène ont démontré des performances mécaniques améliorées avec une bonne stabilité thermique et des profils de dégradation. Ces implants étaient biocompatibles et supportaient l'infiltration, l'adhésion et la prolifération accrue des cellules MC3T3-E1. De plus, la charge d'hématène a considérablement amélioré la puissance ostéogénique des implants en monétite avec des profils de biomarqueurs osseux améliorés avec des agents ostéoinducteurs. Ce travail révèle pour la première fois les potentiels thérapeutiques dérivés de l'hématène et démontre spécifiquement leurs potentiels en tant que prochain grand candidat d'implant pour la régénération du tissu osseux.

## ACKNOWLEDGEMENTS

First and foremost, I would like to thank my supervisors, Dr. Edward Harvey and Dr. Geraldine Merle, for their invaluable guidance and support throughout my graduate studies. Their profound patience and dedication towards the making of this thesis has truly been considerable. Thank you to my committee members: Dr. Louis-Nicolas Veilleux and Dr. Fackson Mwale for their time and counsel, and to our project coordinators, Anne Mathiot and Mary Amedeo. I would like to acknowledge my colleagues at the Montreal General Hospital and Polytechnique, especially Matthew Zakaria and Justin Matta, for their contributions to this project.

## CONTRIBUTION OF AUTHORS

- 1. Rachel Monk** (primary author): responsible for project design, execution, data analysis, literature review, and write-up of manuscript.
- 2. Daniela Vieira** (co-researcher): assisted with experimental planning and execution.
- 3. Justin Matta** (co-researcher): assisted with experimental planning and execution.
- 4. Dr. Edward Harvey** (primary supervisor): provided resources, guidance, and scientific expertise for project design, data analysis, and revision of thesis.
- 5. Dr. Geraldine Merle** (co-supervisor): provided resources, guidance, and scientific expertise for project design, data analysis, and revision of thesis.

## LIST OF ABBREVIATIONS

<b>2D</b>	Two dimensional
<b>3D</b>	Three dimensional
<b>ALP</b>	Alkaline phosphatase
<b>AM</b>	Alamarblue
<b>ANOVA</b>	Analysis of variance
<b>BGLAP</b>	Osteocalcin
<b>b-TCP</b>	Beta-tricalcium phosphate
<b>BTE</b>	Bone tissue engineering
<b>Ca</b>	Calcium
<b>DCPA</b>	Dicalcium phosphate anhydrate
<b>DCPD</b>	Dicalcium phosphate dihydrate
<b>ECM</b>	Extracellular matrix
<b>FBS</b>	Fetal bovine serum
<b>Fe</b>	Iron
<b>GAPDH</b>	Glyceraldehyde-3-phosphate dehydrogenase
<b>GF</b>	Growth factor
<b>GFNs</b>	Graphene family nanomaterials
<b>GO</b>	Graphene oxide
<b>HA</b>	Hydroxyapatite
<b>IONPs</b>	Iron oxide nanoparticles
<b>MCPM</b>	Monocalcium phosphate monohydrate
<b>MOFs</b>	Metal-organic frameworks
<b>NP</b>	Nanoparticles
<b>PCR</b>	Polymerase chain reaction
<b>PBS</b>	Phosphate buffered saline
<b>PS</b>	Penicillin streptomycin
<b>rGO</b>	Reduced graphene oxide
<b>RT-qPCR</b>	Real-time quantitative reverse transcription
<b>RUNX2</b>	Runt-related transcription factor 2
<b>SEM</b>	Scanning electron microscope
<b>SPARC</b>	Osteonectin
<b>TCP</b>	Tricalcium phosphate
<b>XRD</b>	X-ray diffraction

## LIST OF TABLES

**Table 3.1:** Primer sequences used for RT-qPCR.

**Table 4.1:** Summary of scaffold group characteristics assessed by micro-CT<sup>(I)</sup>, SEM/ImageJ<sup>(II)</sup>, and BET<sup>(III)</sup>.

**Table 4.2:** Compressive strength of scaffolds before and after 28 days of dynamic ageing in vitro.

## LIST OF FIGURES

**Figure 1.1:** Schematic of various biological responses to different types of biomaterials.

**Figure 1.2:** Current strategies for the development of different three-dimensional scaffolds.

**Figure 2.1:** Structure of graphene and derivatives.

**Figure 2.2:** Ultrasonic exfoliation from bulk hematite to ultrathin 2D hematene.

**Figure 4.1:** TEM images of ultrathin mono- and bi-layer hematene sheets, and optical image of concentrated hematene.

**Figure 4.2:** XRD of hematene treated and untreated monetite scaffolds before and after 28 days of dynamic ageing in vitro.

**Figure 4.3:** SEM cross-sectional and surface views of scaffold morphology prior to cell culture.

**Figure 4.4:** TGA of hematene treated- and- untreated monetite scaffolds over a temperature range of 25-800 °C at a constant heating rate of 20 °C /min.

**Figure 4.5:** Three-dimensional modelling of constructed scaffolds.

**Figure 4.6:** Scaffold degradation rates over a 28-day period of dynamic ageing.

**Figure 4.7:** Proliferation rates of MC3T3-E1 cells cocultured with scaffolds.

**Figure 4.8:** Viable MC3T3-E1 cells after 7, 14, and 21 days of direct coculture with scaffolds.

**Figure 4.9:** Cross-sectional and surface SEM images of cell-scaffold interactions after 7 and 21 days of culture.

**Figure 4.10:** ALP activity of MC3T3-E1 cells cultured in 3D with hematene treated- and untreated- monetite scaffolds, and in 2D with monolayer cell controls for 7, 14, and 21 days.

**Figure 4.11:** RT-qPCR of osteogenic genes. A) Runx2, master regulator of osteoblast differentiation B) SPARC, non-collagenous protein expressed in mineralized bone matrix.

**Figure S1:** Annotated miller indices of crystalline diffraction planes for monetite.

**Figure S2:** PBS absorption of scaffolds.

**Figure S3:** Standard curve of hematene nanosheets by concentration.

**Figure S4:** Preliminary in vitro biocompatibility testing of hematene nanosheets.



## THESIS INTRODUCTION

Bone tissue possesses a remarkable intrinsic regenerative and reparative capacity in response to injury. However, spontaneous healing at the injury site can be impeded by several factors including extensive bone loss, disease, infection, instability, or inadequate vascularization. In cases of failed or suboptimal healing bone grafts may be used to repair and rebuild bone. Historically, autologous bone has been the clinical standard to bridge the bone defect by supplying all three components of the bone remodeling triad. This triad includes a supply of osteogenic cells, osteoinductive growth factors, and osteoconductive abilities for effective bone repair[1]. Although autografts remain the gold standard of treatment, they are plagued by innumerable drawbacks, such as shortages in supply and high rates of morbidity at donor sites.

Tissue-engineered biomaterial substitutes have matured as viable alternatives. Synthetic substitutes have had attention and momentum over the years, offering clear advantages in availability, workability, sterility, and tunable properties. Despite the developments of polymers and metals as viable options, calcium phosphate cements (CPCs) are recognized as materials available for avascular bone repair. However, CPCs face inherent limitations in their poor resorption rates and low mechanical performances. Since the emergence of dicalcium phosphates, a number of material formulations, setting conditions, and fabrication avenues have been used to heighten resorption mechanisms. While such adjustments have contributed to slight improvements in mechanical performances, they ultimately remain primarily inadequate for weight-bearing applications. With advancing nanotechnology, improvements in biological, mechanical, and electrical properties of engineered constructs are being achieved with state-of-the-art nanomaterial lattices.

In this thesis, we first provide a context for bone physiology, development, and bone healing mechanisms, followed by a review of bone grafting, grafting approaches, and common substitute materials. In the second chapter, we review various nanometals for bone therapy, tactics to leverage physicochemical properties for spatiotemporal control, and highlight the emergence of an ultrathin, two-dimensional material class that may revolutionize biomedical applications. The third chapter uncovers materials used in our research where we highlight the success of monetite in bone regeneration and draw attention to the unique physicochemical properties and emerging biomedical applications of a newly discovered ultrathin nanomaterial- hematene. In the final two

chapters, we include our study hypothesis and objectives as we harness and bridge hematene nanosheets with a monetite implant to elevate biological functionality and mechanical strength. We conclude this thesis with a discussion of the prospective future of hematene derivatives as a scaffold candidate for bone regeneration and identify encouraging avenues to corroborate this therapeutic potential.

## **CHAPTER 1: BONE GRAFTING AND BONE SUBSTITUTES**

### **1.1 BONE GRAFTING**

Bone tissue has a remarkable intrinsic regenerative capacity for skeletal development and healing from injury. However, spontaneous healing can be impeded by a number of issues such as disease, infection, improper fixation, or insufficient vascularization at the injury site of critical defects. In cases of failed or suboptimal healing, bone grafts are used to augment healing. Depending on the type, surgical technique, and application, bone grafts can facilitate distinct biological and mechanical responses for the production of new bone at the host-graft interface. There have been many structural, functional, and mechanistic forms developed each with their own advantages and disadvantages. They can be broadly classified based on their material source being natural (autografts, allografts, and xenografts) or synthetic (metals, ceramics, polymers). Traditional grafting procedures use bone tissue harvested from either the patient directly, a cadaver, or a human donor for transplant into a bone defect. While native bone is the best choice for grafting due to its viable cellular machinery, these advantages are in part negated by the severity and extent of the complications associated with its harvest.

Autografts continue to remain the standard in bone grafting procedures with their all-encompassing osteoconductive, osteoinductive, and osteogenic properties for successful bone repair. Traditional approaches involve harvesting bone from various skeletal regions of the same patient including the proximal tibia, distal radius, greater trochanter, and more commonly the iliac crest, for surgical transplant[2]. Despite providing notable fusion rates[3], conventional autografts have faced considerable shortages due to their limited bone supply and high donor site morbidity[4, 5].

The use of allogenic bone has developed as the next best avenue that can be obtained from human cadavers or living donors. Despite their lack of osteogenic properties, allografts have

overcome several of the disadvantages of autografts. Principle advantages lie in their low donor site morbidity and shorter operation times due to not requiring a second surgical site for its harvest. They can be obtained in various forms such as cortical, cancellous, corticocancellous, and processed bone derivatives (demineralized bone matrices) that are predominantly osteoconductive[6]. Allografts can also exhibit variable osteoinductive and mechanical performances that are highly dependent on their preservation methods of freezing (fresh frozen), or freeze-drying (processed)[7]. However, concerns of disease transmission, immune rejection, graft costs, and high failure rates are still maintained[8-10].

Xenografts are another option that similarly eliminates the donor site complications of standard autografts. In this approach, bone is primarily acquired from porcine or bovine animal models for transplant into humans for similar reparative aims. Xenografts are widely known to have the added benefits of being cheaper and more readily accessible than autologous and allogenic bone. However, they are highly disadvantaged by their physical properties in being materials that are both brittle and lack toughness which can make them prone to failure[11]. While considered an inferior option to autografts, there are contradictory reports on how xenografts perform relative to allografts[12-14]. Allografts are still preferred over xenografts. Xenograft has more widespread use in dental and maxillofacial surgery than orthopaedics, with use typically only for intra-articular defects and revision arthroplasty. While also sharing similar complications to allografts, infection is the most frequently reported xenograft-related complication[15].

## **1.2 BONE TISSUE ENGINEERING**

Bone tissue engineering is a multi-disciplinary field that encompasses material science, engineering, and clinical medicine with aims to provide a less invasive and widely accessible alternative to natural bone grafts through engineered bone tissue[16]. The sensitivity and adaptability of biological cells to cues in their physical surroundings have allowed biomaterial-based therapeutic strategies to flourish. The fundamental capacity of biomaterials to induce different host tissue responses has been accredited to the fundamental differences in material properties. Since the emergence of first-generation biomaterials in the 1960's, subsequent generations have steadily improved biological responses with greater material functionality and tissue specificity[17].

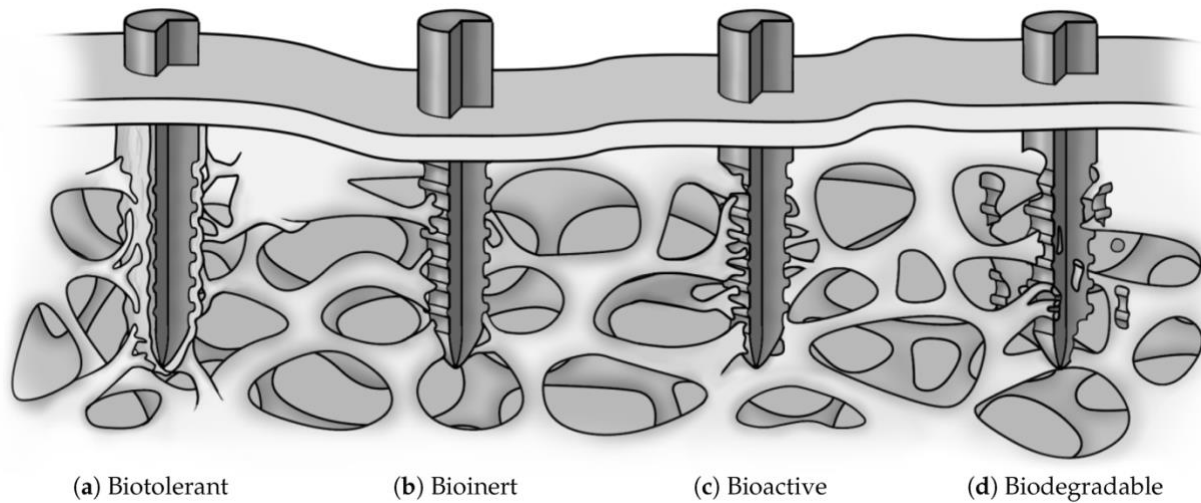


**Figure 1.1:** Schematic of various biological responses to different types of biomaterials [18]

It is well known that the functionality and durability of the implant type can impact the severity and extent of tissue responses. *Bioinert*, biologically inactive materials, have very minimal host reactions when placed in the physical body. Biomaterial retention is commonly achieved through mechanical integration or fibrous encapsulation without any chemical reactions, although integration with adjacent host tissue is possible under certain conditions[19, 20]. The most biocompatible orthopaedic implant materials include highly bioinert titanium and its alloys (zirconia, alumina). *Biotolerant* materials are a second option that involves fibrous encapsulation from chemical reactions between the implant and tissue. The thickness of the fibrous layer can be induced by factors such as ion release and corrosion products from the material surface[21]. Stainless steel (SS), cobalt-chromium-molybdenum alloys (CoCrMo), and the majority of synthetic polymers can be categorized as biotolerant. Contrary to bioinert and biotolerant material categories, *bioactive* materials interact directly with their surrounding environments to produce specific biological responses. Bioactive materials include glasses, ceramics, and polymers. These materials have highly reactive surfaces that can facilitate a chemically and biologically bonded interface for cell attachment and tissue development[22, 23]. Some of the most widely advertised options include *biodegradable/bioresorbable* materials that are naturally degraded by the body over time to replace surrounding tissue. Bioresorbable implants have presented with appropriate fixation stability comparable to metallic-based materials[24] and require no second surgery for implant removal. Unlike permanent implants, biodegradable materials are associated with

decreased risks of foreign body reactions (FBR) and chronic inflammation due to their controlled degradation and complete elimination after defined periods[25, 26]. However, if degradation kinetics are not optimized, then product toxicity can further amplify inflammation[27]. While these findings have contributed significantly to the understanding of the biointerface, a wealth of interest currently surrounds novel combinations of bioactive and biodegradable materials for nanocomposite and scaffold advancements.

### **1.2.1 Tissue engineered scaffolds**

Tissue-engineered three-dimensional (3D) scaffold matrices are being engineered with growth factors and cells with the intent to stimulate and support native repair mechanisms. They can be designed in many different shapes, sizes, and forms from a variety of materials such as metals, natural and synthetic polymers, composites, and calcium phosphate bioceramics. In the selection of a biomaterial, material features (i.e. topographical features, chemical compositions, crystallinity), host tissue requirements (i.e. tissue type, strength, size, shape), and reaction at the tissue-material interface is imperative to consider[28]. Third-generation frameworks have become leading strategies to advance biomaterial properties through the combinations of resorbable and bioactive bioceramics. Now in recent years, the focus has shifted to the fabrication of fourth-generation biomimetic scaffolds.

Several biofabrication strategies have been developed in an attempt to mimic the biochemical, biophysical, and biomechanical cues of the native extracellular matrix to appropriately provide the necessary cues for functional regeneration (Figure 2.2)[29]. Attention to the structural features of the scaffold is imperative for a successful application, as grain size, pore structure, and surface topography are acknowledged as major passive cues that can dictate cell behavior and fate[30, 31]. For scaffolds to meet the objectives of bone repair, they must be engineered in a way that satisfies certain biological, mechanical, and structural criteria.

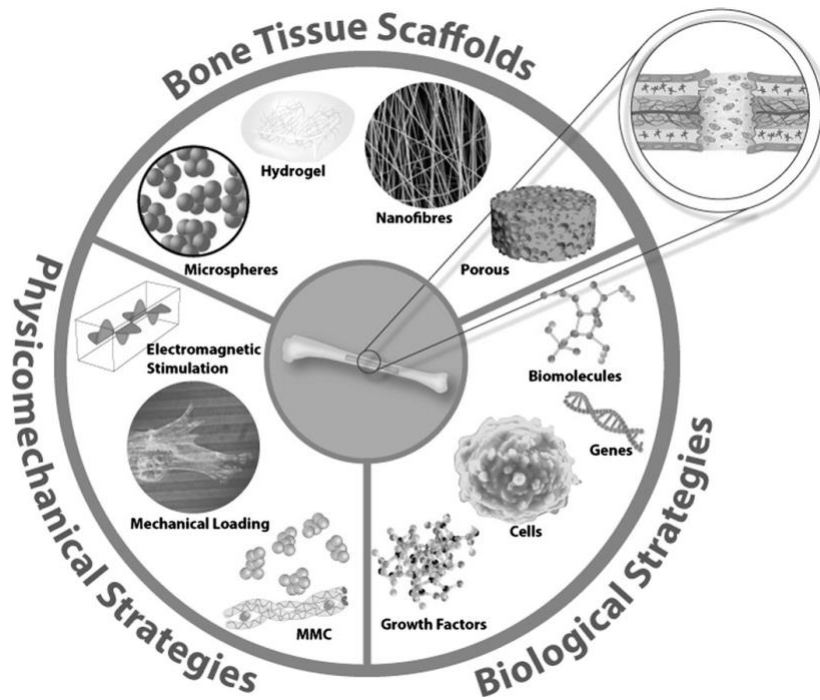


**Figure 1.2:** Current strategies for the development of different 3D scaffolds [32]

### 1.2.2 Scaffold requirements

#### I) Biological

Biocompatibility is the first prerequisite for any biomaterial substitute. Biocompatibility can be defined as the capacity to fully interact with a host free of adverse effects that include toxic or immunological responses[33]. Bone scaffolding materials should also be biodegradable to adequately support the native remodeling processes of the ECM[34]. To do so, it is imperative that the degradation rate of the biomaterial closely match the ingrowth of new tissue. Scaffolds that degrade too quickly can cause the accumulation of toxic by-products, and interfere with the repair of the defect site by removing its structural framework[35]. On the contrary, those that degrade too slowly can provoke an inflammation response that can lead to host rejection[36]. Though this has been difficult to control from an engineering perspective, contributing factors that largely impact material degradation have included material composition, structure, surface topography, and environmental cues[37, 38].

Successful bone healing using bone grafts or substitute materials involves three general mechanisms of action that constitute the regeneration triad: osteogenesis, osteoinduction, and osteoconduction. Ideal bone scaffolds should display osteoconductive

and osteoinductive properties. Osteoconductive materials serve as a 3D scaffold that promotes the deposition of new bone through favorable interactions at the biointerface (i.e. cell adhesion, migration, infiltration, proliferation)[6]. Osteoinduction is the process that induces osteogenesis through the stimulation of immature osteoprogenitor cells to differentiate into mature osteoblasts for new bone formation[39]. It is the process that native bone is highly dependent on following trauma for healing, and the component that is often the most challenging to achieve for tissue engineering strategies. Other strategies to investigate the osteoconductive properties in novel biomaterial systems involve the direct supplementation of growth factors that stimulate host tissue growth.

## **II) Mechanical**

Biomechanical stability is an imperative factor to attain complete union during the bone healing process[40, 41]. Surgical techniques for bone stability and healing can include manipulation of misaligned bony fragments by ‘resetting/reducing’ them and/or reinforcement with orthopaedic hardware. Compression plating is one method to introduce rigidity and absolute stability that encourages primary healing without callus formation[42]. When bone fragments are not rigidly stabilized (i.e. intramedullary nailing and bridge plating methods), at best a greater amount of callus tissue forms, which increases susceptibility to non-union or delayed healing[42-44].

Tissue-engineered scaffolds must have the physical integrity to outperform a variety of mechanical stressors that are encountered at the implant site. To effectively support the growth of native tissue over and within the construct, scaffolds must have mechanical properties that closely match the host tissue. The mechanical properties of native bone have depended considerably on its components and hierarchical structural organization[45] which has been exceedingly difficult to fully recreate. BTE strategies often try to find a middle ground between the porosity and mechanical performance of the engineered construct when fabricating the scaffold microstructure. The most common mechanical tests include tensile and compressive strength, especially for bioceramic cements. Engineered scaffolds should have compressive strength values that either fall in the 2-12 or 130-205 MPa range of native trabecular or cortical bone, respectively[46-48]. Though tensile strength is difficult to measure in brittle materials, it has been reported to be on average 10% less than the compressive modulus[49].

### III) Structural

The native ECM contains topographical and adhesive features within the nano- and microscale range that drastically influence cell phenotype. The physical environment of an ECM analog should guide cells toward their normal physiological behavior by providing appropriate physical cues in its geometry, size, surface chemistry, and organizational features[50]. These elemental components of the scaffold architecture have been known to define mechanical and osteoconductive properties, degradation rates, vascularity, and the extent of interaction with cells[51, 52]. It should have the capacity to facilitate nutrient delivery and waste removal, as well as support cell adhesion, migration, growth, and proliferation[53]. To fulfill these criteria, highly porous designs with open and interconnected pores have been found to be crucial for sufficient permeability and mechanical interlocking with the surrounding tissue[54, 55].

Fiber diameter and pore size are two architectural features that have dominated the topographical landscape with mesh-like nanoscale structures[56]. To mimic the dominant fibrous network of ECM tissues, it has been recommended that fibrous scaffolds are engineered with diameters in the range of 50 to 500nm for adequate functionality[57]. Electrospinning of microfiber/nanofiber-polymer blends is one technique that has been shown to achieve fibrous scaffolds with dimensional and geometrical similarities.

Pore size should be large enough to support bone and vascular network formation, with appropriate distributions for biological support at any point of the construct. Though some cells tend to prefer smaller pore sizes (ie. fibroblasts), it has been reported that osteoblasts (10-50 microns) prefer larger sizes in the range of 100-200 microns for successful mineralization[58]. While there has been no definitive requirement, the general recommendation of pore size falls around 100 to 500 microns[59].

The surface topography and chemistry of a scaffold are also important. Some surface features to consider are wettability, roughness, and specific surface. The roughness of a material's surface can govern interactions at the biointerface and directly influence morphology, proliferation, and phenotype expression. Microrough surfaces have shown to be ideal for osteogenic differentiation and tissue bonding, though profile shape (waviness, coatings, finish) can have a large effect[60-62]. Another feature important for cell attachment to the surface is the wettability of a construct which is influenced by chemical composition and surface energy[63]. Wettability is defined as the ability of a liquid to spread over a materials surface, which can be quantitatively measured by the



water contact angle. Materials that are hydrophilic (i.e. high surface energy) have lower contact angles ( $<90^\circ$ ) and good wettability that is crucial for optimal cell adhesion at the material interface[64].

### **1.3 SYNTHETIC BONE GRAFT SUBSTITUTES**

The scientific community has made great progress in developing a number of avascular bone substitutes from synthetic biomaterials. Over the years, synthetic matrices with osteoinductive or osteoconductive properties have presented in various forms, shapes, and sizes for versatile applications. Synthetic matrices with osteoinductive or osteoconductive properties offer ideal advantages in terms of their workability, sterility, and tunable material properties for diverse bone-targeting applications[65]. Popular synthetic-based scaffold biomaterials have included polymers, metals, and calcium phosphate-based bioceramics. These can be used alone or combined with other material additives to optimize biomaterial functionality and biological performance. While polymers are noteworthy options, calcium phosphate-based ceramics have been more preferred in bone repair studies due to their superior tissue responses[66-68]. In the context of this thesis, a central overview of calcium phosphate-based bioceramics is provided with metals highlighted in the subsequent chapter.

#### **1.3.1 Calcium phosphate-based bioceramics**

Porous calcium phosphate-based bioceramics exemplify some of the most extensively studied materials for bone repair due to their compositional resemblance to native bone minerals. They are highly advantageous with their setting reactions, bioactivity, and biological performances. While these materials are predominantly osteoconductive, advances in bone tissue engineering have enabled the developments of osteoinductive ceramics by manipulating chemical compositions, structural parameters, topographical features, and particle sizes[69, 70]. Other avenues have frequently blended bioactive ceramics with natural polymers to achieve better constructs that fit scaffolding requirements. These bioactive cements can be divided based on their bioresorption profiles. Hydroxyapatite (HA), dicalcium phosphate- dihydrate (DCPD), and anhydrate (DCPA) are the three most commonly used in bone repair studies.

## **I) Hydroxyapatite ( $\text{Ca}_{10}(\text{PO}_4)_6(\text{OH})_2$ )**

Hydroxyapatite (HA) is a naturally occurring calcium phosphate mineral that is present in both teeth and bones. HA is an ideal material choice for bone repair based on its resemblance to bony apatite which composes 60% of native bone[71]. It also presents the advantage over brushite setting reactions in that apatite cements are set at neutral pH values. Though HA is an inherently brittle material with low tensile strength and fracture toughness, it exhibits very good compressive strength that is often dependent on grain size[72, 73]. During the fabrication process, sintering temperatures and particle sizes can be manipulated for better microstructural control. Caution in manufacturing must be used as it has been reported that sintering at high temperatures (~1200-1450 °C) can lead to the loss of functional groups that promote decomposition to  $\alpha$ -TCP,  $\beta$ -TCP, and TTCP which can ultimately hinder densification and mechanical strength[74, 75]. While all appreciable, the success of HA in bone repair has been considerably limited by its low-negligible resorption rates associated with apatite CPCs[76]. Avenues to advance HA performances have involved the blending of HA and polymers with some success. Alternate avenues have turned to faster settings, highly reactive, and better resorbable options such as dicalcium phosphates.

## **II) Brushite ( $\text{CaHPO}_4 \cdot 2\text{H}_2\text{O}$ ) and Monetite ( $\text{CaHPO}_4$ )**

Dicalcium phosphates, brushite (DCPD) and monetite (DCPA), have evolved as some of the most attractive orthopaedic materials for bone augmentation. These state-of-the-art bioresorbable ceramics have acquired considerable interest owing to their biomimicry, metastable nature in physiological fluids, and resorptive profiles[77]. As potential scaffold candidates, they demonstrate good osteoconductive and osteoinductive capabilities for bone repair[78-80]. Their strong bone repair potentials have been shown in a variety of forms including, injectable pasts, granules, coatings, and now scaffolds. Though sharing chemical similarities, monetite and brushite exhibit distinct behaviors.

Brushite cements are easily precipitated at a low pH ( $\text{pH} < 6$ ) via mixing monocalcium phosphate monohydrate (MCPM),  $\beta$ -tricalcium phosphate ( $\beta$ -TCP), and water[77]. The MCPM/ $\beta$ -TCP and power/liquid (P/L) ratios have shown the capacity to change cement properties, largely mechanical strength, after setting. It has been demonstrated that a P/L ratio of 3:1 exhibits ideal setting behaviours for brushite with improved mechanical strength and physical integrity with less fragmentation compared to 1:1 P/L cements[81]. However, the thermodynamic tendency to convert to a more stable and slow resorbing apatitic phase *in vivo* is well recognized[82-84]. While

these observations have not been true for monetite, pre-set brushite cements are readily being utilized as precursors for monetite transformation under water-deficit conditions[85]. Bioceramic autoclaving is one thermal treatment that provides ideal dehydrating conditions (temperature, pressure, humidity) to prevent bulk shrinkage of the material while increasing pore size[86]. It also has shown to yield considerable improvements resorption and osteogenicity of the monetite cement when compared to its brushite precursor[87], dry heated monetite, and HA[88].

Monetite has developed great popularity in tissue engineering as a potential frontrunner among calcium phosphate phases. Monetite is one of the fastest resorbing calcium phosphate phases in bone repair studies[81, 89] and has exhibited remarkable bone healing abilities[90]. Monetite has been recognized for its successful ability to increase the quantity of bone regenerated[88, 91], provoke intense osteogenic differentiation earlier[89], and exhibit superior resorbability[80]. When combined, graphene-monetite scaffolds have demonstrated the superior ability to enhance bone growth and regeneration *in vitro*[92]. While monetite and brushite still both remain restricted to non-weight bearing applications similar to other calcium phosphates, the research community is discovering novel avenues for mechanical advancements.

## **CHAPTER 2: NANOMATERIALS IN BONE TISSUE ENGINEERING**

### **2.1 INTRODUCTION**

Nanomaterials are defined as having at least one external dimension between 1 and 100 nanometres. They can be categorized based on their type (inorganic, organic, carbon, or composite) or dimensionalities (0D-3D). These nanoscale strategies have all gained considerable momentum in effective bone repair with nanotechnology-centered smart scaffolds already in development. Nanomaterials offer an abundance of advantages with their tunable physiochemical properties for different biological, mechanical, and structural strategies. Of particular interest is their highly unique quantum size effects, large surface areas, and self-assembly contingent on intrinsic material features[93, 94]. Their small-scale physical elements, with those materials that are electrically and optically active, exhibit highly promising potentials to mimic the nanofeatures of bone for better regulation and bone repair. One area of significant attention has been the bone-targeted delivery of drugs, growth factors, and genes by exploiting nanomaterials with good loading and release mechanisms[95, 96]. Other strategies have included activating the electrical, magnetic, and

thermal properties of select nanomaterials for initiating different signaling pathways for better bone regeneration. For the purpose of this chapter, the longstanding use of metal-based- and recently evolving 2D- nanomaterials for bone repair strategies will be reviewed and highlighted.

## 2.2 METAL NANOSTRUCTURED PARTICLES

Iron and zinc are essential micronutrients for growth, development, and immune functions within the human body. They are respectively classified as the first and second most abundant trace metals in the body[97]. In light of this, a wealth of research in basic science has been devoted to understanding their involvement in bone metabolism.

### I) Zinc

Zinc (Zn) preferentially localizes to bones and has been shown to increase as bone mineralization increases[98, 99]. This has been attributed to ALP, the major regulator of bone mineralization, using zinc as a cofactor. It has also been observed that in response to bone trauma, Zn levels specifically rise in tissue at the injury site[100, 101]. The stimulatory effects of Zn in collagen production[102], bone formation[102, 103], and bone mineralization have been corroborated by many *in vivo* and *in vitro* models having similar findings. In bone tissue engineering, Zn has been used alongside other substitute materials of ceramics, metals, and polymers.

Qiao et al. used plasma immersion ion implantation and deposition to load Zn onto the sub-surface of TiO<sub>2</sub> to investigate its osteogenic potential. When cultured with stem cells, Zn-doped implants revealed an improved osteogenic effect with higher ALP activity and osteogenic-related gene expression (OCN, Col-I, Runx2) compared to TiO<sub>2</sub> alone and ‘bulk-doped Zn’[104]. After implantation in a rat model for 12 weeks, Zn-doped implants demonstrated good osseointegration and Zn release profiles, along with early-stage bone formation showing a large bone contact ratio compared to controls[104]. While infection rates continue to remain higher after medical device implantation, the use of zinc oxide (ZnO) nanoparticles could be explored as an alternative option with its antimicrobial nature [105, 106].

Zinc has also been incorporated within CPCs to have both chemical compositions similar to bone and ions that regulate its metabolism. With this aim, Li et al. used Zn-doped HA powders with different molar ratios (0.25, 0.5, 1) for combination with poly(propylene fumarate) to fabricate a PPF-Zn-HA nanocomposite scaffold. In this study, findings revealed that all Zn-based

nanocomposite scaffolds supported higher cell proliferation, ALP activity, and ECM mineralization in MC3T3-E1 cells relative to HA/PPF control[107]. It was also observed that the scaffolds with 0.5 molar ratios displayed the highest ALP activity and mineralization[107]. While the authors report previous findings on the mechanical profiles for the PPF/HA scaffolds, changes to the mechanical properties of the scaffold from Zn additions were not investigated in this study.

## **II) Iron**

Hemoglobin, an iron-containing metalloprotein, provides oxygen to tissues and cells, which are necessary for their survival and regeneration. The influence of iron (Fe) on bone metabolism has been investigated using iron- restrictive, deficient, or overloaded models. Under these conditions, it has been reported that bone formation and resorption are significantly reduced, leading to low bone mineral density (BMD) and weakening [108-110]. Fe has also been reported to influence collagen synthesis and vitamin D metabolism that are two key elements in bone healing[111, 112].

Iron oxide nanoparticles (IONPs) have in fact developed as the top studied FDA-approved nanomedicine for drug delivery, magnetic resonance imaging, and most commonly as iron-replacement therapies[113]. With this diverse profile, it is obvious that IONPs are strong candidates for translational medicine. In tissue engineering, they are highly regarded due to their intrinsic biocompatibility, chemical stability, and highly tunable material features. Wang et al. examined the capacity of IONPs to promote osteogenic differentiation of stem cells through gene microarray assays and bioinformatics analysis. It was observed that IONPs had a preference for the mitogen-activated protein kinase pathway, and its downstream genes were regulated to promote osteogenic differentiation[114]. Similarly, Hu et al. used 10mg/mL superparamagnetic iron oxide nanoparticles (SPIONs) loaded in a gelatin sponge scaffold that was implanted inside rats (n=81) for 2 and 4 weeks. In keeping with the previously reported findings, SPIONS displayed the ability to induce osteogenesis, however, here the degradation of the scaffold and host interaction was interestingly monitored over time with MRI[115]. While this approach could be of benefit to localize the nanoparticles in real-time for clinical modifications, the feasibility of the approach would have to be further clarified. Other publicized efforts have found that IONPs can induce osteoblast differentiation better when subjected to a static magnetic field (SMFs) than used alone[116]. This combinational approach has not only been shown to synergistically enhance osteogenic differentiation with its hyperthermic effect upon application but also help disperse

IONPs with the magnetic field to prevent aggregation[117]. Of added benefit to address surgical site infections is their excellent antimicrobial performances against *S. aureus* and *P. aeruginosa*, which has demonstrated to kill up to ~90% of bacteria with just 0.050g/ml concentration[118].

## **2.3 TWO-DIMENSIONAL NANOMATERIALS**

Crystalline materials that have two dimensions (XY plane) outside of the nanometric range and have an atomic-scale thickness (Z plane) are classified as two-dimensional[119]. These materials are however not confined to the nanoscale. To date, various methods have emerged for 2D material synthesis that can be classified as ‘bottom up’ or ‘top down’. While the former uses atomic or molecular precursors to react and grow to produce nanoscale materials, the latter has involved the controlled separation (exfoliation) of bulk materials. Of the two, top-down strategies are viewed as more scalable, cost-effective, and useful for the preparation of ultra-thin, high-quality nanosheets[120]. Physical-based methods involve the application of a mechanical force or ultrasonic wave to separate the layered nanosheets into ultrathin mono-, bi- or multi-layer sheets. Common examples include micromechanical exfoliation, shear exfoliation, and ultrasonic exfoliation. The method and organic solvent used for separation are two factors that can largely influence nanosheet dispersion, long-term stability, and thickness[121, 122].

### **2.3.1 Graphene-family nanomaterials**

#### **I) Graphene**

Graphene exists as a single or multi-layer of aromatic carbon atoms arranged in a two-dimensional honeycomb lattice. It is renowned for sparking a material revolution after its immaculate isolation from naturally occurring crystalline carbon. Graphene has one of the largest specific surface areas ( $2640 \text{ m}^2/\text{g}$ ) in the 2D material family that is second only to metal-organic frameworks ( $1000\text{-}10,000 \text{ m}^2/\text{g}$ )(MOFs)[123]. Of particular interest for orthopaedic applications is graphene’s notoriously high tensile strength which is reported to be 130 GPa, which is 200 times higher than steel[124, 125]. In addition to its exceptional mechanical properties, graphene also outcompetes carbon with its thermal and electrical conductivity  $5000 \text{ m}^{-1}\text{K}^{-1}$  [126] and  $6000 \text{ S/cm}$ [127], respectively. With introductions as the thinnest, lightest, and strongest material to date[125, 128, 129], it has quickly become a popular choice for bioimaging/biosensing[130], drug delivery[131], and tissue engineering[132].

Graphene is an exceptional scaffold candidate in BTE strategies with its remarkable mechanical profiles, excellent electrical conductivity, and surface functionality. These highly desirable features have been harnessed a number of ways to augment bone healing. Some strategies have used graphene's electrical properties to activate mechano-transduction pathways for greater induction of osteogenic activity[133]. Other methods have exploited the special chemical reactivity of graphene's planar structure to load drugs and biomolecules for bone-targeted and antibacterial delivery systems[134]. Over the last decade, bone repair strategies have focused on the more favourable graphene-derivatives of graphene oxide (GO) and reduced graphene oxide (rGO).

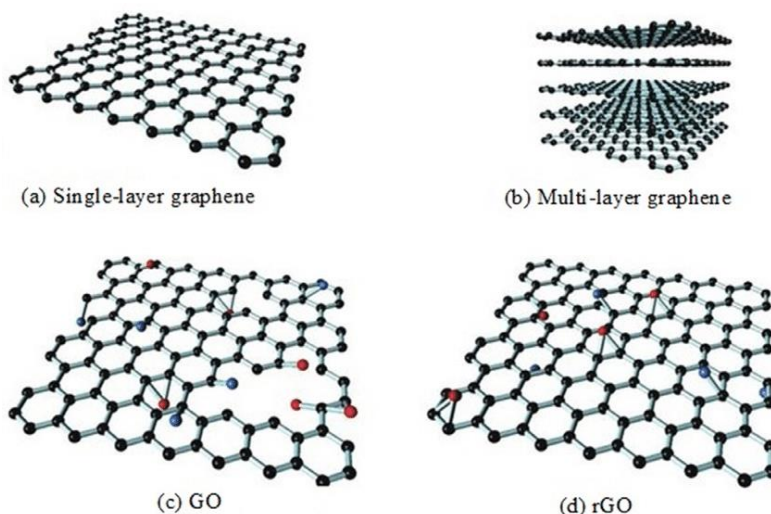


**Figure 2.1:** Different structures of graphene and its derivatives GO and rGO [135]

## II) Graphene oxide (GO)

Graphene oxide is prepared from the oxidation of graphite-to-graphite oxide followed by subsequent exfoliation. While GO has maintained similar chemical properties to graphene, the oxygen functional groups distributed over the surface have given it different physical properties. It has been reported that during graphite oxidation, the graphene sheets lose their conjugated double bonds which result in undesirable thermal and electrical conductivity properties compared to graphene[136]. This reduction in thermal conductivity has been by almost 2-3 orders of magnitude[137]. The specific surface area of GO has also presented to be much smaller (2630 m<sup>2</sup>/g)[138]. However, evidence has suggested that the electrical conductivity of GO nanosheets

could increase by modifying the oxygenated functional groups on its surface during synthesis[139, 140].

On the contrary, GO is typically favored over graphene as a more admirable candidate for biofunctionalization. This has been due to its surface polarity, hydrophilicity, and good dispersion in aqueous solutions[141, 142]. With its cheap and easy workability, GO has been used in many studies for the fabrication of innovative composite systems to enhance bone repair mechanisms. Particularly, it has been an attractive reinforcement material for brittle polymers that have incompatible mechanical profiles for biological applications. In effort to improve cell attachment, proliferation, and mechanical characteristics of polylactic acid (PLA), Belaid et al. examined the effects of 0.3% (w/w) GO within a 3D printed polylactic acid (PLA) scaffold. Compared to PLA alone, GO was found to significantly improve scaffold strength by 30% and upregulate proliferation and mineralization in an osteosarcoma cell line[143]. Saravanan et al. used a similar GO concentration (0.25%) within a chitosan (CS) and gelatin (Gn) scaffold and found that GO notably improved osteogenic differentiation of rat osteoprogenitors and accelerated bridging of a rat tibial bone defect[144].

### **III) Reduced graphene oxide (rGO)**

rGO is obtained from GO reduction through electrochemical reduction, chemical reduction, or thermal reduction methods. While the chemical reduction to reduce GO can offer good scalability, it often is at the expense of electrical conductivity and surface area of the end-product rGO. Other more favorable approaches such as thermally reducing GO at  $>1000^{\circ}\text{C}$ [145] have shown to produce rGO with high surface areas similar to pristine graphene. Considering the dispersibility of graphene is inversely proportional to physical properties, rGO has presented with a better dispersion than GO but less than pristine graphene. rGO has demonstrated substantial improvements in material constructs through reinforcements, combinations, or more advanced avenues or through harnessing their physiochemical features to stimulate alternative bone healing pathways.

In an attempt to provide scaffolds with bone-mimicking properties, Bahrami et al. developed rGO-coated collagen scaffolds through crosslinking and freeze-drying. rGO was selected for scaffold design based on its greater porosity (94%) than GO (83%) when combined with collagen [146, 147]. Not only did the rGO provide a large surface area for cell adhesion with no reported cytotoxicity, but it increased the mechanical strength 2.8 times greater than without rGO



reinforcement[146]. When scaffolds were implanted in a cranial bone defect for 12 weeks, it was found that rGO additives significantly enhanced bone formation compared to the control[147]. Similar improvements were noted in a study by Abazari et al. that used 1% rGO as a filler for magnesium (Mg)-ZM31 alloy biocomposites. Here it was found that rGO incorporation improved compressive strength ( $282.3 \pm 9$  MPa) and failure strain compared to the Mg alloy alone ( $244.5 \pm 9$  MPa)[148]. rGO at 0.5 and 1 wt% demonstrated to have higher levels of ALP activity when cultured *in vitro*, in addition to eliciting an antimicrobial effect on *E. coli* and *S. aureus*[148].

#### **2.3.1.1 Toxicity of graphene-family nanomaterials**

Several reports have drawn attention to the differential cytotoxicity of graphene-family nanomaterials in biological systems. This has been attributed to the differences in material synthesis and design parameters used. The cytotoxicity associated with the graphene family can be influenced by a number of features and parameters.

Sizable evidence has commonly reported dose- and time-dependent cytotoxic effects within *in vitro* and *vivo* models. Yoon et al. examined the size-dependent cytotoxic effects of graphene nanoflakes on HeLa cell lines through bioassays and electrochemical impedance. Findings suggested that smaller-scale graphene nanoflakes ( $30.9 \pm 5.4$  nm) compared to larger-scale nanoflakes ( $80.9 \pm 5.5$  nm) promoted greater apoptosis and ultimately induced greater toxicity[149]. Similarly, Wang et al. examined dose-dependent effects of GO nanosheets on human fibroblasts over a range of 5-100  $\mu$ g/mL for 5 days, and the cytotoxic effects of 100, 250, 400  $\mu$ g administered *in vivo* using mice models through tail vein injections. It was shown here that GO concentrations of more than 50  $\mu$ g/mL were cytotoxic to human fibroblasts, and doses of just 400  $\mu$ g in mice induced chronic toxicity shown by granuloma formation and/or death (44%)[150]. Further correlations have been observed between cellular toxicity and surface chemistry[151], as well as shape (i.e. layer versus nanotube)[152].

#### **2.3.2 Novel 2D Hematene**

Since the advent of graphene in 2004, modern 2D nanomaterial discoveries and nanotechnology-driven strategies continue in early developmental phases. More recently added to the 2D material family is hematene; an atomically ultrathin nanosheet of iron oxide measuring three atoms thick, synthesized from bulk hematite ( $\alpha$ -Fe<sub>2</sub>O<sub>3</sub>). While iron oxides have long-established photothermal and regenerative abilities, hematene exhibits rare properties attributed to

its dimension. Though its bioresorbable nature is noteworthy, what is of most significance in the materials development is the rare 3D bonding networks that the majority of 2D materials do not develop when synthesized from bulk precursors[153]. This extremely unique property makes hematene an exceptionally strong material. Its bulk-hematite counterpart is antiferromagnetic, but hematene is a ferromagnetic material that can produce a strong magnetic effect by aligning its magnetic moments with the field[153, 154]. With these properties, the magnetic domains of hematene will remain aligned even after the removal of a magnetic field which could introduce a high level of flexibility for advanced biomedical therapies. On the contrary, SPIONs are highly explored avenues for drug delivery and bone repair applications that show magnetic properties only in the presence of an external magnetic field. Hematene's ultrathin nature with its magnetic and semiconductive features has attracted significant attention in the field of spintronics for the development of nanoscale devices[155]. What's more is that with their planar structure, 2D materials pose superior electrocatalytic reactivity attributed to their high surface area and greater presence of active sites to move electrons[153, 156, 157].

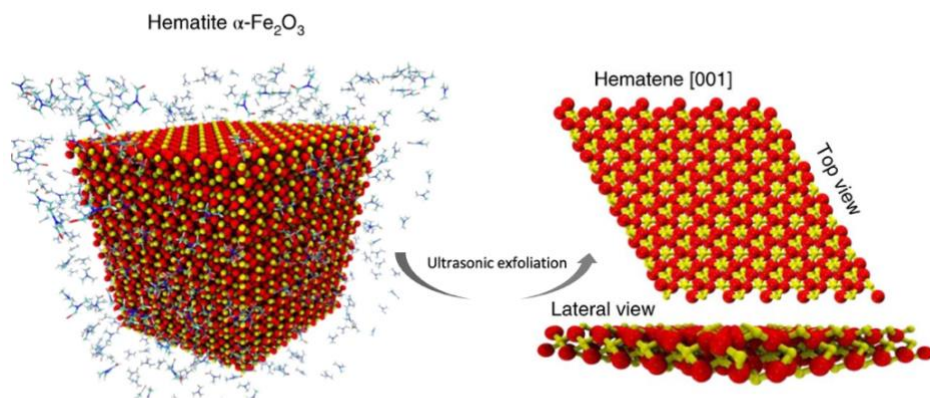


**Figure 2.2:** Ultrasonic exfoliation from bulk hematite to ultrathin 2D hematene [153]

## 2.4 NANO-DOPED CALCIUM PHOSPHATE CEMENTS

The use of nanomaterials within CPCs has developed as a very common method to optimize bone implants and scaffolds due to their unique properties. Nano-driven composite systems can offer advantages for bone research by incorporating the desirable compositional features of CPCs with highly functionalized modern materials. Identifiable advantages are demonstrated to enhance

bioactivity and osteoinduction properties of CPCs through nano-driven strategies. These features have been of specific interest within IONP-CPC systems, though 2D nanomaterial systems could now offer an all-encompassing approach to bone repair. Of 2D materials options, rGO has presented as the most readily explored option within graphene and its derivatives, with a number of significant research around its combination with CPCs.

A number of *in vitro* and *in vivo* studies show support of IONPs for bone repair avenues. Xia et al. constructed a novel composite of IONP-doped chitosan/CPCs at different concentrations (1%, 3%, and 6%) to investigate bone biomarker protein and mRNA expressions in human dental pulp stem cells (hDPSCs). It was observed that 3% IONP (~9nm Ø) incorporation doubled the flexural strength and significantly enhanced cement bioactivity as evidenced by a greater osteogenic effect[158]. It was thought that the IONPS induced a more attractive hydrophilic surface for better protein adsorption that contributed to this activity[158]. Previous reports within this group have also shown that magnetically responsive IONP-CPCs can be harnessed under SMF exposure to increase cell proliferation, bone mineralization, amount of ALP activity, and osteogenic bone marker expressions[159]. Similar strategies have utilized the advanced electrical properties of 2D nanomaterials in an effort to elicit greater responses at the biological level. For example, Seonwoo et al. incorporated rGO for the structural reinforcement of brittle calcium phosphate cements and applied pulsed electromagnetic fields (PEMFs) to promote osteogenic differentiation. It was reported that the chemical bonding of rGO-CPC significantly increased the mechanical properties of the cement, and most importantly, the rGO-CPC composite exhibited high rates of osteoinductivity and osteoconductivity with enhanced osteogenic differentiation via application of PEMFs[160].

Graphene family nanomaterials also exhibit remarkable osteogenic properties on their own without external stimulation. Lee et al. combined rGO with HA at  $10\mu\text{g mL}^{-1}$  to form hybrid composites as an alternative avenue to bioactive scaffolds. It was shown that MC3T3-E1 cells underwent spontaneous osteodifferentiation with sustained proliferative activity[161]. *In vitro* findings of improved ALP activity and mineralization was corroborated with a calvarial defect model that supported the addition of rGO to significantly enhance new bone formation when compared to HA alone[161]. When applied to more complex 3D systems for implantation into rat calvarial defects, rGO loading on a biphasic calcium phosphate scaffold showed to induce greater amounts of new bone volume ( $\text{mm}^3$ ) [162].

Dicalcium phosphates (DCPs) are increasingly climbing toward some of the most popular bioactive cements in bone repair studies. Pan et al. fabricated an iron-doped brushite cement to examine the functionality of this construct in its osteoconductive and antimicrobial abilities. Though additions of iron improved ALP activity and osteogenic-related genes, prolongation of the time for cement setting with higher degradation and more injectable profiles were noted[163]. It was also observed that this construct inhibited the growth of gram-negative and positive bacteria[163], suggesting that iron-doped brushite has strong potentials for both antimicrobial and regenerative applications. Similar efforts in an attempt to augment the mechanical properties of brushite cements introduced GO at 0, 0.5, 2, and 5% weight into the cement directly, to yield a GO/DCPD cement upon setting[164]. It was found that the addition of GO nanosheets improved compressive strength compared to pure DCPD alone[164]. In this study, good cell adhesion with a human osteosarcoma cell (MG63) was noted, however, GO concentrations were negatively correlated to cell viability with the strongest cytotoxic effect demonstrated with 5%GO[164]. In keeping with the majority of the literature, GO was found to significantly enhance ALP activity[164]. While it is recognized that IONP-, and especially GO-nanomaterial combinations with DCPs are less abundant in the literature, this can in part be attributed to an incomplete exploration of DCPs and graphene family nanomaterials owing to their later introductions.

## **CHAPTER 3: HEMATENE-DOPED MONETITE SCAFFOLD FOR BONE REPAIR**

### **3.1 RATIONALE**

Autografts remain the gold standard for the repair of bone defects, however, concerns of limited availability, donor site morbidity, and increased surgical times are maintained. Synthetic constructs with osteoconductive or osteoinductive abilities are being explored as alternative avenues. Three-dimensional scaffolds have developed as some of the most advanced and effective tissue engineering approaches that can be constructed using biofactors, cells, and highly selective materials. Dicalcium phosphates are a highly favorable option due to their compositional resemblance to native bone, metastability in physiological fluids, and advanced resorptive profiles. Monetite in particular has developed considerable attention as one of the fastest resorbing calcium phosphate (CaP) phases in bone repair studies with remarkable healing performances.

Nanomaterial lattices are now being used to fine-tune the mechanical and biological performances of scaffold systems. Graphene, a 2D atomic layer of carbon is an example of a well-publicized material that has improved the strength, functionality, and osteogenic potency of a variety of scaffolds with its dimensional properties. However, conflicting concerns of poor bioresorption and concentration-dependent toxicity have questioned their translational potential. Hematene, a novel 2D nanosheet of iron oxide has introduced an unconventional route to 2D material discovery with its 3D bonding networks. While iron oxides have long-established their photothermal and regenerative abilities, hematene exhibits utterly distinct unique optical, magnetic, electrical, and mechanical properties attributed to its dimension. In this work for the first time, we explore the osteogenic potency of a novel biodegradable hematene-doped scaffold for orthopaedic bone repair.

### **3.2 HYPOTHESIS**

Following a comprehensive review of the literature and understanding of material properties, we hypothesized that the bioactive potential of hematene combined with monetite would significantly improve bone formation through the enhanced expressions of osteogenic bone biomarkers compared to monetite alone.

### **3.3 STUDY OBJECTIVES**

1. To design a hematene reinforced monetite scaffold for the regeneration of bone
2. To identify the optimal hematene to monetite ratio that generates the greatest osteogenic effect
3. To determine whether this novel implant can significantly accelerate and improve osteogenic differentiation of MC3T3-E1 pre-osteoblastic cells
4. To determine whether osteoinductive agents contribute significantly to the rate of hematene-induced osteogenesis

## 3.4 EXPERIMENTAL SECTION

### 3.4.1 Materials:

#### Synthesis of hematene nanosheets

2D hematene nanosheets were prepared using a previously established protocol adapted by our colleagues[157]. Briefly, 150mg of bulk hematite ( $\alpha$ -Fe<sub>2</sub>O<sub>3</sub>) powder was distributed within 200mL of acetonitrile (ACROS organics; AC167650010)[165]. The solution was sonicated for 48hrs followed by probe sonication for 1hr at 40% amplitude (130 watts, Sonics Vibracell). To separate unexfoliated materials, the supernatant was collected following centrifugation at 4000 x g for 10 minutes. The organic solvent was removed through centrifugation and the pelleted nanosheets were dispersed in a 50% (v/v) ethanol solution and renewed three times for washing. After washing, hematene nanosheets were concentrated in Milli-Q ultrapure water and sterilized for biocompatibility studies.

#### Preparation of Monetite-0.5Hematene scaffolds

Monetite (Dicalcium phosphate anhydrous, DCPA) cements were prepared as per Sheikh et al[81]. Briefly,  $\beta$ -tricalcium phosphate ( $\beta$ -TCP) (Mereck) and monocalcium phosphate monohydrate (MCPM)(ABCR, EmbH & Co.KG) was combined using a ratio of 1.2 to 1 respectively. The powder was mixed until homogenous, combined with distilled water at a 3:1 power to liquid (g/mL) ratio, and kneaded until firm in a cylindrical mold (5.5mm  $\varnothing$  x 2.5mm ). Samples were left at 40°C for 24hr in a vacuum oven to form hard brushite. Hydrothermal dehydration of brushite to monetite ensued 35 minutes of autoclave treatment at 120°C, 100% humidity, 15 psi. To remove the porogen, cements were immersed in culture medium followed by PBS for 24hr and left to dry at 40°C overnight prior to decoration. Hematene nanosheets were homogenously distributed over monetite cements at 0.5% (w/w) through centrifugation at 3000 x g for 4 mins. Similar parameters were followed for uncoated monetite cements in distilled water. Scaffolds were allowed to dry overnight at 40°C prior to being autoclaved for sterilization.

### **3.4.2 Characterizations:**

#### **Transmission electron microscopy (TEM)**

The morphological structure of hematene nanosheets was investigated by high resolution bright-field transmission electron microscopy (TEM, FEI Tecnai F20, 200 kV, Hillsboro, OR, USA) at an accelerating voltage of 2 kV.

#### **X-ray diffraction (XRD)**

To evaluate the crystalline structure of hematene and the uncoated- and coated DCPA scaffolds, X-Ray Diffraction (XRD) was performed using a diffractometer (Bruker EIGER2 R 500K) at 40kV, 40mA, with Cu Ka ( $\lambda = 1.51 \text{ \AA}$ ) radiation. The samples were scanned in a  $2\theta$  range of  $10^\circ$  to  $50^\circ$  with a step size of  $0.02^\circ$ .

#### **Scanning electron microscope (SEM)**

The morphology and surface topography of the coated and uncoated scaffolds were evaluated with a scanning electron microscope (SEM, Inspect F50, FEI Company, Hillsboro, OR, USA). The samples were cut, coated with a thin layer of  $0.05\mu\text{m}$  platinum and examined at an accelerating voltage of 2 kV.

#### **Thermogravimetric analysis (TGA)**

TGA was used to quantify the amount of hematene coated on the scaffold surface and the thermal decomposition profiles using a SDT Q500 instrument (TA Instruments, DE, USA). The TGA instrument was operated under nitrogen atmosphere over a temperature range from room 25 to  $800^\circ\text{C}$  with a ramp rate of  $10^\circ\text{C} \cdot \text{min}^{-1}$ .

#### **Brunauer-Emmett-Teller Method (BET)**

The specific surface area (SSA) of the uncoated and coated scaffolds in their cylindrical 3D form was determined using the BET method. Samples were dried, degassed, weighed, and analyze with helium adsorption-desorption (TriStar 3000, Micromeritics).

#### **Micro-computed tomography ( $\mu\text{CT}$ )**

Architectural features of the scaffolds were captured using micro-computed tomography for quantitative morphometric analysis. The  $\mu\text{CT}$  images were acquired with the following parameters: 50 kVp, 160  $\mu\text{A}$ , 8W, and 0.5 mm aluminum filter. Acquisition parameters were set with a rotation step of 0.50 (deg), exposure time of 3790 ms, and two frame-averaging. Images were reconstructed using 40% beam hardening and ring artifact with a reduction of 4. A region of

interest of 565 x 565 pixels was used for thresholding and filtering. Anisotropic diffusion filter was applied to reduce noise (iterations (8), gradient (10)) with global thresholding to segment the pores from the scaffold. Binary operations included removal of all but the largest objects through sweep despeckling followed by removal of noise less than 20 voxels from pores. 3D morphometrical analysis was provided by which scaffold porosity (%) was calculated as 100 – percent object volume for each sample assessed (n=2). Manual calculations of pore size from SEM images were corroborated with a series of CT slices using Data Analyzer Software for accuracy.

### **3.4.3 Absorption, decomposition, and mechanical testing:**

#### **Fluid absorption**

To investigate the absorption capacity of cylindrical scaffolds, the PBS uptake test was carried out adhering to previously established protocols[166, 167]. Scaffolds were fully submerged in 1 mL of PBS (pH = 7.4) and incubated at  $37 \pm 1^\circ\text{C}$  until saturation. The scaffolds were removed from PBS at each timepoint of interest, blot dried to remove excess liquid and weighed ( $W_w$ ). The dry weight of each scaffold was recorded prior to immersion ( $W_d$ ). The swelling rate percentage was calculated using the following equation (2):

$$(1) \text{ PBS uptake (\%)} = (W_w - W_d / W_d) \times 100$$

#### **Degradation behaviour**

Degradation behaviour of scaffolds were examined over 28 days using dynamic ageing protocols. Briefly, scaffolds were immersed in PBS solution (Gibco™) at  $37 \pm 1^\circ\text{C}$  using a liquid to cement volume ratio of 60 as per our colleagues[168]. To achieve *vivo*-like conditions, PBS was refreshed daily with 1h of gentle agitation using a rocking platform (Cole Parmer, IL, USA) similar to previous degradation protocols [169, 170]. At days 7, 14, 21, and 28 scaffolds were removed from the ageing medium, dried overnight at  $40^\circ\text{C}$ , and weighed to determine mass loss as a function of time (1). Relative residual mass percentage was calculated from triplicate samples and averaged. Following 28 days of ageing, scaffolds were tested for changes in crystallinity and compressive strength.

$$(2) \text{ Degradation rate (\%)} = (W_0 - W / W_0) \times 100$$

#### **Compressive strength**

The compressive strength of scaffolds was evaluated before and after 28 days of *in vitro* ageing. Samples were made in triplicate, weights recorded, and mounted on the testing machine



(5544, Instron) perpendicular to the lower anvil. The maximum compressive load before failure was tested using a 100N load cell at a constant crosshead displacement rate of 1mm/min.

#### **3.4.4 *In vitro* testing:**

##### **Cell culture**

Murine calvarial osteoblast cell lines MC3T3-E1 (subclone 14) was purchased from ATCC (Manassas, VA) and maintained in basal alpha-MEM (Minimum Essential Media  $\alpha$ , Gibco™) supplemented with 10% Fetal Bovine Serum (FBS)(Gibco™) and 1% Penicillin-Streptomycin (P/S) (Gibco™). Cells were passaged when reached 75% confluency and used at a maximum of passage 7 for all experiments. Cells were stained with trypan blue and counted using a hemocytometer when having reached a 90% confluency at the desired passage number. Scaffolds were left to soak in complete culture medium under sterile conditions for 1h to promote cell attachment for plating. For all *in vitro* tests, MC3T3-E1 cells were micro-seeded on top of scaffolds at a seeding density of  $5 \times 10^4$  and left to adhere in a 37°C, 5% CO<sub>2</sub> environment for 30 minutes prior to flooding with basal media. The next day, cells were washed twice with PBS and replenished with osteogenic-conditioned media supplemented with 50µg/mL ascorbic acid and 10mM  $\beta$ -glycerophosphate. The cells were cultured for 21 days with growth medium changes every 2-3 days.

##### **Cell viability and proliferation**

AlamarBlue™ Reagent (Invitrogen™) was used to assess material-cell biocompatibility and proliferative effects in 2D and 3D cultures. This method uses the reducing environment of viable cells to convert resazurin to resorufin, a highly fluorescent red compound representative of metabolically active cells. Cell proliferation was examined at days 1, 3, 5, and 7, while cell viability measurements were acquired prior to gene analysis at days 7, 14 and 21. At the respective timepoints, a fresh working solution of culture media supplemented with 10% alamarBlue® was gently incubated with the treated and non-treated conditions for 1h (viability) and 3h (proliferation) at 37 °C protected from light. Following the incubation period, triplicate readings from each sample (n=3) was pipetted into a 96-well plate to measure fluorescence at 560/590 (excitation/emission). Cell proliferation was normalized to baseline measures (day 0) and represented relative expressions. Cell viability was normalized to the untreated monolayer controls and represented as a mean percentage following subtraction of background values.

## **Cell adhesion**

Scaffold adhesion and changes to cell morphology was examined with SEM at days 7 and 21 with the previously outlined parameters. To prepare samples for imaging, scaffolds were removed from culture media and washed twice with PBS. Scaffolds were subjected to a series of graded alcohol dehydrations following fixation overnight with 4% paraformaldehyde at 4°C. Scaffolds were left to dry overnight at 40°C, sputter-coated with a thin layer of platinum and viewed by SEM.

## **Alkaline phosphatase (ALP) activity**

ALP activity was measured using a highly sensitive colorimetric assay kit (83369; abcam). This method examines the extent of dephosphorylation of the substrate p-nitrophenyl phosphate (pNPP) by ALP which generates a yellow product. The intensity of color formation can be quantified through absorption at 405nm and interpreted for ALP activity. Adhering to the procedural manual at days 1, 7, 14 and 21, cell supernatant without phenol red was collected in triplicate and analyzed directly within the standard range. The activity present in each sample was determined by correcting background absorbance and dividing the amount of pNPP detected (by the sample volume (mL) and reaction time (min)).

## **Real-time quantitative reverse transcription (RT-qPCR)**

RNA was extracted and purified using TRIzol (Invitrogen) and RNeasy spin columns with on-column Dnase treatment (Qiagen) adhering to manufacturer's instructions at days 7, 14, and 21. The concentration and quality of RNA were measured using a NanoDrop™ 2000 Spectrophotometer system (NanoDrop Technologies, Thermo Scientific™). 25ng of RNA was used for the reverse transcription and amplification using a one-step QuantiNova™ SYBR Green RT-PCR kit (Qiagen) using an Applied Biosystems™ StepOne™ Real-Time PCR System. Biological and technical triplicates were subjected to cycling conditions of 10 min at 50°C, 2 min at 95°C, 5s at 95°C, and 10s at 60°C for 40 cycles. The expression for each gene of interest (Table 3.1) was normalized to GAPDH expression. Relative expressions were calculated using the  $2^{-\Delta\Delta CT}$  method with untreated monetite as the calibrator.

### **3.4.5 Statistical analysis**

Statistical significance was assessed using the SPSS software platform (IBM, NY, United States) where  $p \leq 0.05$  was accepted as statistically significant. Differences between treated and

untreated/control groups were compared using independent paired t-tests. Paired t-tests were used to examine same-group differences over time. One-way ANOVA with tukey adjustment was used to compare data sets with greater than two groups.

**Table 3.1:**

Primer sequences used for RT-qPCR

Gene	Forward Sequence (5' to 3')	Reverse Sequence (5' to 3')
<b>RUNX2</b>	ACCCCTCCTATCTGAGCCAG	GCCCAGTTCTGAAGCACCTG
<b>SPARC</b>	CCAACCCAGTCCAGGTGGAA	GGCAGGAAGAGTCGAAGGTCTT
<b>GAPDH</b>	AGTGTTTCCTCGTCCCGTAG	GAGGTCAATGAAGGGGTCGT

## CHAPTER 4: RESULTS

### 4.1 CHARACTERIZATIONS:

#### 4.1.2 Transmission electron microscopy (TEM)

Bright-field TEM confirmed the successful exfoliation of ultrathin mono- and bi-layer hematene nanosheets with a mean lateral size of 150 nm (Figure 4.1). High-resolution TEM imaging identified the hexagonal symmetry of hematene aligned on the 001-zone axis (**Figure 4.1b**) with lattice parameters of  $\alpha=0.249$  nm,  $c=0.680$ nm in accordance with the previously established  $c/\alpha$  ratios [171].

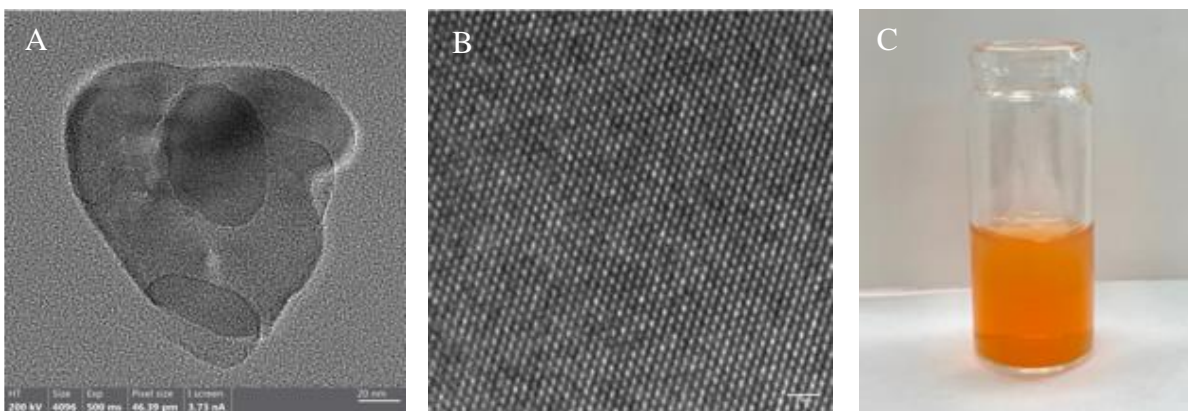


**Figure 4.1: Confirmation of 2D hematene.** TEM (A) and high-resolution TEM (B) images with ultrathin mono- and bi-layer hematene sheets with a mean lateral size of ~150nm (C) Optical image of concentrated hematene solution.

### 4.1.3 X-ray diffraction (XRD)

Phase purity of the 3D scaffolds before and after *in vitro* ageing was confirmed via XRD. Scaffolds with and without hematene were in good agreement with the crystalline diffraction of monetite that confirmed the successful phase conversion from its brushite precursor (**Figure 4.2**). The fully annotated miller indices of the hexagonal diffraction planes for monetite are shown in FigureS1 that is in accordance with the JCPDS (ICDD) database card 09-0080. Crystalline diffraction patterns following 28 days of ageing remained consistent with the pre-ageing spectra between and within scaffold conditions. No phase changes or phase impurities were identified.

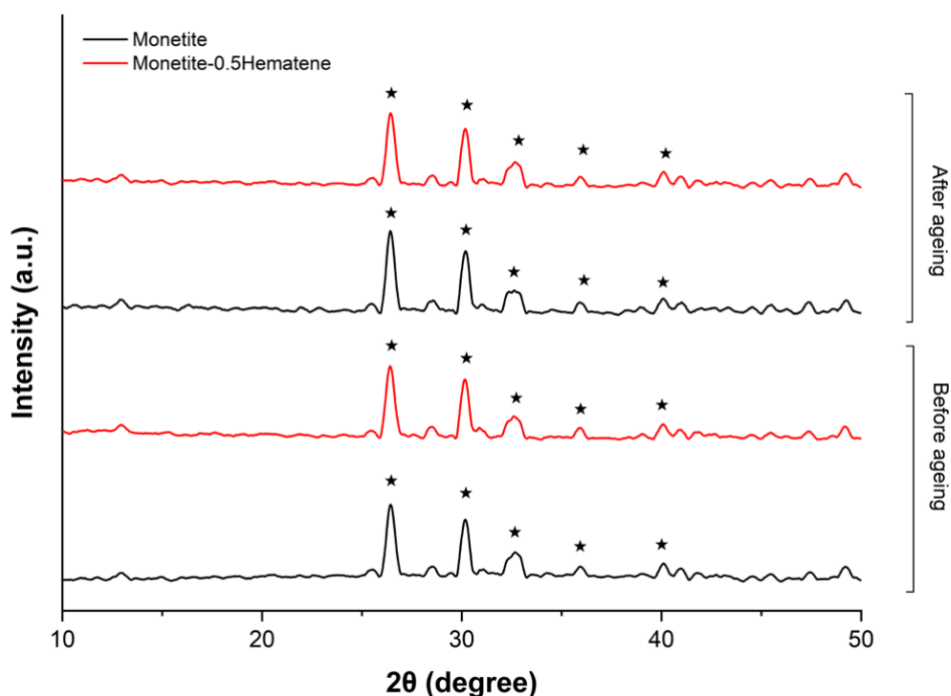


**Figure 4.2: X-Ray Diffraction Spectra** of hematene treated (red) and untreated (black) monetite scaffolds before and after 28 days of dynamic ageing *in vitro*. Conversion from DCPD to DCPA is indicated (\*) with miller indices of 200, 120, 02, 02, 003 (left to right).

### 4.4.4 Scanning electron microscope (SEM)

The effect of hematene loading on scaffold architecture was examined by SEM. SEM images of scaffolds showed a typical rectangular, plate-like morphology that was maintained between uncoated and coated conditions. As expected, a change in the surface topography of the treated scaffolds was seen due to the presence and homogenous distribution of hematene nanosheets over

the monetite surface that can be seen in **Figure 4.3**. It was also observed that the nanosheets remained on the exterior surface without having penetrated the scaffold interior.

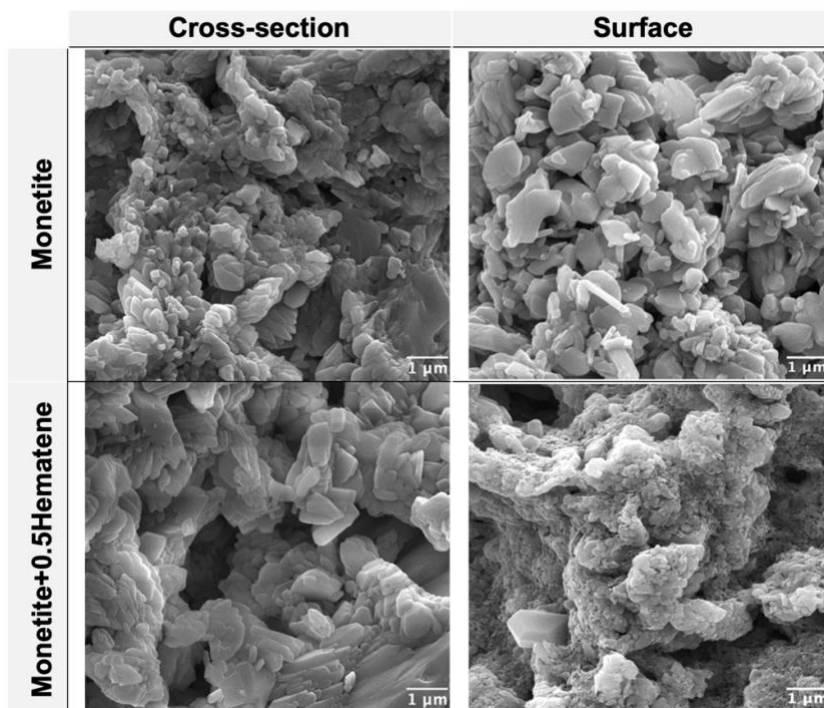


**Figure 4.3: SEM images.** Cross-sectional and surface views of acellular scaffolds showing the typical rectangular, plate-like morphology that is consistent with monetite at a magnification of 10x.

#### 4.1.5 Thermogravimetric analysis (TGA)

Thermal treatment showed that initial weight loss up to 280 °C was minimal that accounted for 1%. Substantial weight loss of the scaffolds started at 280°C and continued until approximately 465°C. Throughout this period of steep decline, a greater degree of mass loss was observed for the hematene loaded scaffolds (7.2%) due to oxide decomposition when compared to its pure monetite counterpart (6.8%)(**Figure 4.4**). Mass loss ceased at approximately 700 °C with a residual mass of 92.1% and 91.5% for monetite and hematene-loaded scaffolds, respectively. A high degree of thermal stability was maintained without being significantly impacted by hematene loading.

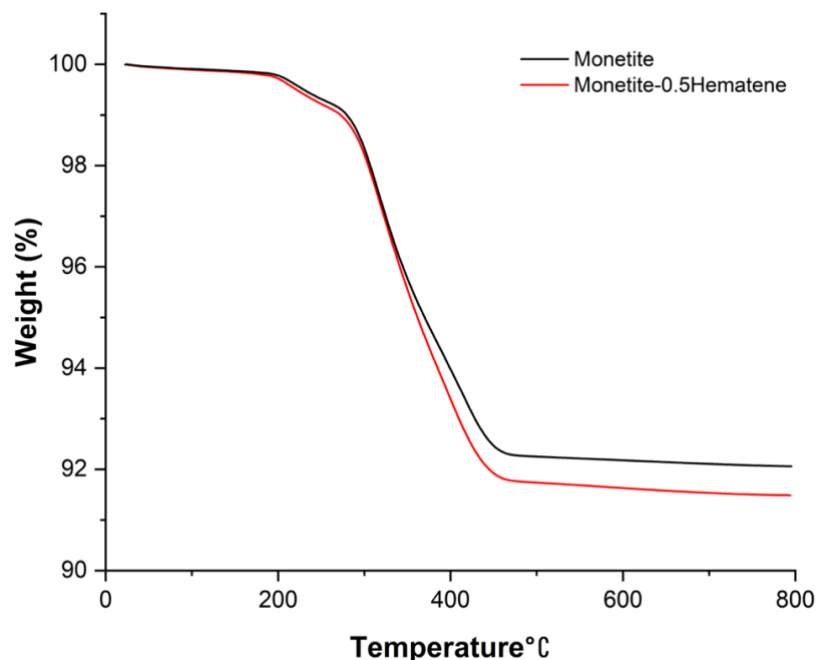


**Figure 4.4: TGA.** Thermodynamic behaviour of treated (red) and untreated (black) scaffolds over a temperature range of 25-800 °C at a constant heating rate of 20 °C /min.

#### 4.1.6 Micro-computed tomography (micro-CT)

Scaffold morphology using SEM and micro-CT images revealed a multi-porous scaffold with majority of pore size distributions in line with macroporous materials. Hematene-treated and untreated scaffolds respectively demonstrated an average pore size of  $114 \pm 10$  and  $139 \pm 19$  that was validated for accuracy between methods. Similar reductions with respect to average porosity were also seen in the hematene loaded scaffolds that is noted in **Table 4.1** and can be visualized in **Figure 4.5 D1-D2**. Nanosheet loading at 0.50% of scaffold weight demonstrated to reduce pore size and porosity by 19.76% and 8.89%, respectively, when compared to the pure monetite control.

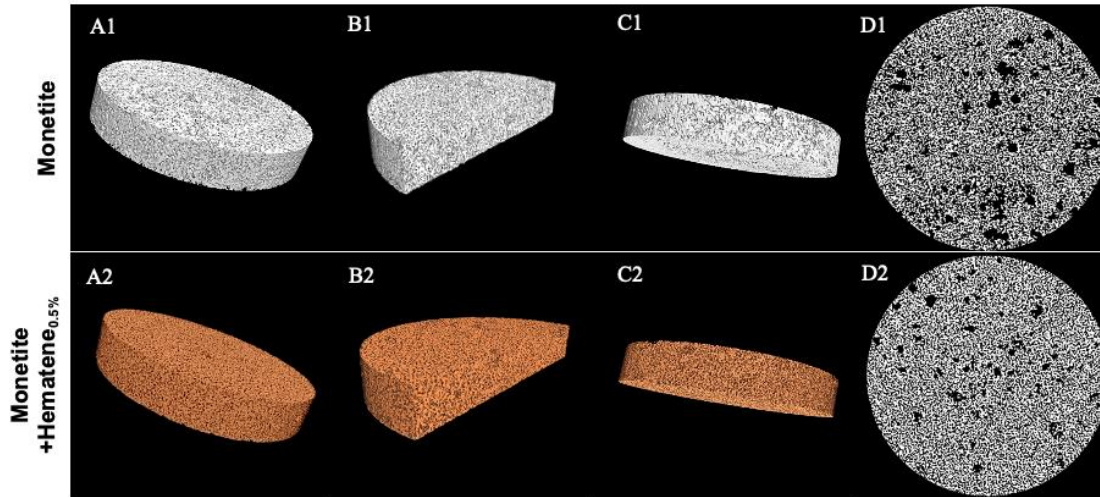


**Figure 4.5: 3D modeling of constructed scaffolds.** Micro-CT reconstruction of pure monetite (**A-1,2,3**) and hematene-loaded monetite (**B-1,2,3**) scaffolds. High-resolution 3D imaging showing multipoint views (**1**), cross-sectional views (**2**), and side views (**3**). Representative 2D micro-CT binary images showcasing the changes in hematene-loaded cement porosity (**B4**) from monetite controls (**A4**).

**Table 4.1:**

Summary of scaffold characteristics assessed by micro-CT<sup>(I)</sup>, SEM/ImageJ<sup>(II)</sup>, and BET<sup>(III)</sup>  
Data presented as mean  $\pm$  standard deviation

Parameter	Monetite	Monetite-0.5Hematene
<sup>(I)</sup> Porosity (%)	$47 \pm 1.10$	$43 \pm 0.35$
<sup>(II)</sup> Pore size ( $\mu m$ ) **	$139 \pm 19$	$114 \pm 10$
<sup>(III)</sup> Specific Surface Area ( $m^2/g$ )	$5.07 \pm 0.13$	$5.24 \pm 0.19$

\*\* denotes statistical significance at the 0.01 level

#### 4.1.7 Degradation behaviour

Hematene-monetite scaffolds aged *in vitro* presented with degradation profiles that were well matched to monetite controls (**Figure 4.6**). Hematene loaded scaffolds lost on average 10.9% of its original mass that was in accordance with the 10.5% lost by monetite controls after 28 days of ageing in PBS. The physical integrity of both scaffold groups was maintained gradually over a 4-week period with a consistent weekly degradation rate of 2.7% that was observed in parallel. Aside from having demonstrated a significantly smaller mass loss over the first 7 days ( $2.8 \pm 0.44$

versus  $3.6 \pm 0.11$ ), hematene-treated scaffolds thereafter remained largely unchanged to monetite controls with good degradation profiles.

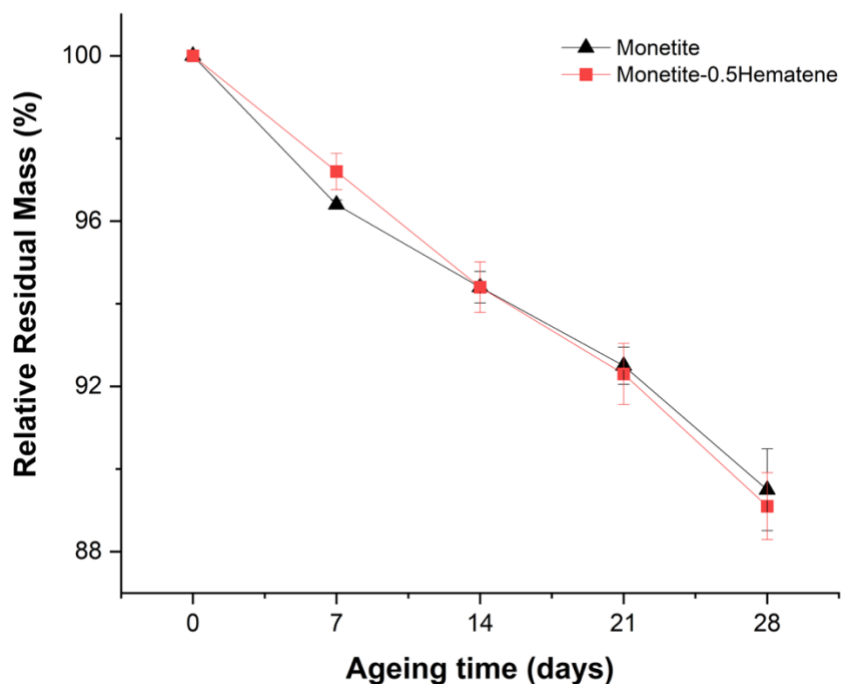


**Figure 4.6: Scaffold degradation.** *In vitro* degradation rates of hematene treated (red) and untreated (black) monetite scaffolds (n=3) over 28 days of dynamic ageing. Data presented as mean  $\pm$  standard deviation.

#### 4.1.8 Compressive strength

Mechanical strength testing prior to *in vitro* ageing showed that hematene loading significantly improved scaffold compressive strength by 18% compared to the pure monetite control (**Table 4.2**). The mechanical integrity of the fabricated scaffolds was then evaluated with dynamic ageing protocols for 28 days in PBS. Expectedly, within-group compressive strength decreased significantly from pre-ageing values but there were no significant differences detected between groups after the 28 days of *in vitro* ageing. It was observed that the monetite scaffold architecture irrespective of hematene-loading lost on average 12% of its original strength without being compromised after 4 weeks of *in vivo*-like conditions.



**Table 4.2:** Compressive strength of scaffolds (n=3) before and after 28 days of dynamic ageing *in vitro*. Data presented as mean  $\pm$  standard deviation.

	Compressive Strength (MPa)	
	Day 0	Day 28
<b>Monetite</b>	2.90 $\pm$ 0.08 **	2.64 $\pm$ 0.26
<b>Monetite-0.5Hematene</b>	3.47 $\pm$ 0.13 **	3.02 $\pm$ 0.67

\*\*p  $\leq$  0.01

## 4.2 IN VITRO FINDINGS

### 4.2.1 Cell proliferation

The proliferation rates of MC3T3E1 cells cocultured in 3D on treated or untreated scaffolds were investigated at days 1,3,5, and 7 with the alamarBlue Reagent. Samples at each timepoint were normalized to their respective baseline readings, averaged, and represented as a mean relative expression. While there was no significant difference detected between groups after 24h, hematene-treated scaffolds displayed a significant 1.28-, 1.33-, and 1.27- fold increase in proliferation relative to monetite controls at days 3, 5, and 7, respectively (**Figure 4.7**). At the end of the 7-day period, the proliferative activity of MC3T3-E1 was 24% greater when cultured with hematene-treated scaffolds. These results suggest that hematene-monetite scaffolds can support and enhance cellular activity.

### 4.2.2 Cell viability

Cell viability at days 7, 14, and 21 was investigated to detect differences in number of metabolically active cells prior to RNA extraction. Cells exposed to the hematene-treated scaffolds exhibited a mean cell viability (%) of 88.9  $\pm$  11, 90.5  $\pm$  5.1, and 87.0  $\pm$  2.5 that was relative to the monolayer control at days 7, 14, and 21, respectively (**Figure 4.8**). Untreated monetite displayed similar viability readings with an observed mean of 82.5  $\pm$  0.6, 93.2  $\pm$  8.8, and 92.0  $\pm$  2.1 at the timepoint of interest. While both scaffold groups showed good biocompatibility with cell viability above 80% across all timepoints, treated and untreated scaffold groups showed a significant reduction relative to cell monolayer controls at day 21. No significant differences were otherwise noted on days 7 and 14.

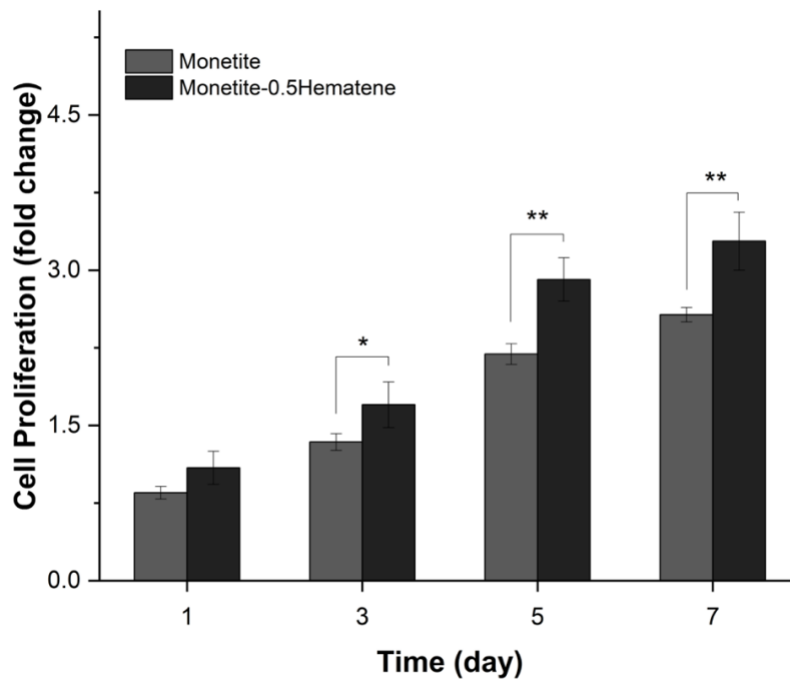


**Figure 4.7: Cell Proliferation.** Proliferation rates of MC3T3-E1 cells cocultured on treated or untreated scaffolds (n=3) for 1, 3, 5, and 7 days. Data represented as relative fold-change from baseline (day 0). Both scaffold groups demonstrate an appreciable increase in fluorescent intensity over time that is consistent with sustained proliferative activity. Data presented as mean  $\pm$  standard deviation.

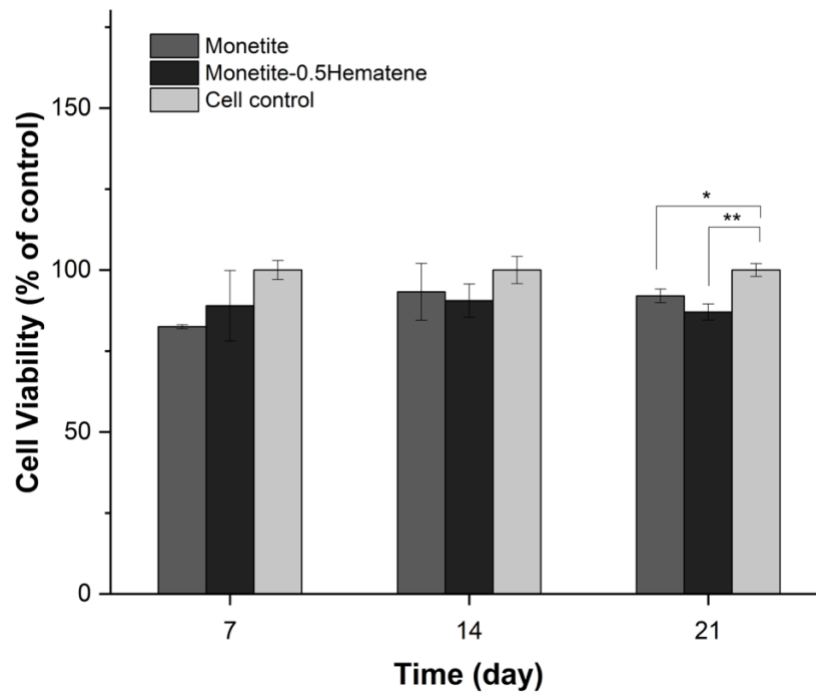


**Figure 4.8: Cell Viability.** Mean percentage of viable MC3T3-E1 cells after 7, 14, and 21 days of direct coculture with scaffolds (n=3). Treated and untreated scaffolds were highly biocompatible with cell viability  $> 70\%$  when normalized to the untreated 2D monolayer controls. Data presented as mean  $\pm$  standard deviation.

### 4.2.3 Cell adhesion

SEM images captured on days 7 and 21 of *in vitro* culture confirmed the successful cell attachment to both control and hematene-treated scaffolds with good cell infiltration and distribution (**Figure 4.9**). Morphological observations of MC3T3-E1 cells included a fibroblast-like shape with cytoplasmic projections on day 7. By day 21, osteogenic differentiation was substantiated by the considerable presence of calcium nodules that suggested mature osteoblastic activity. It was also observed that the hematene-loaded scaffolds exhibited an observable difference with greater cellular adhesion on its exterior surface compared to monetite scaffolds.

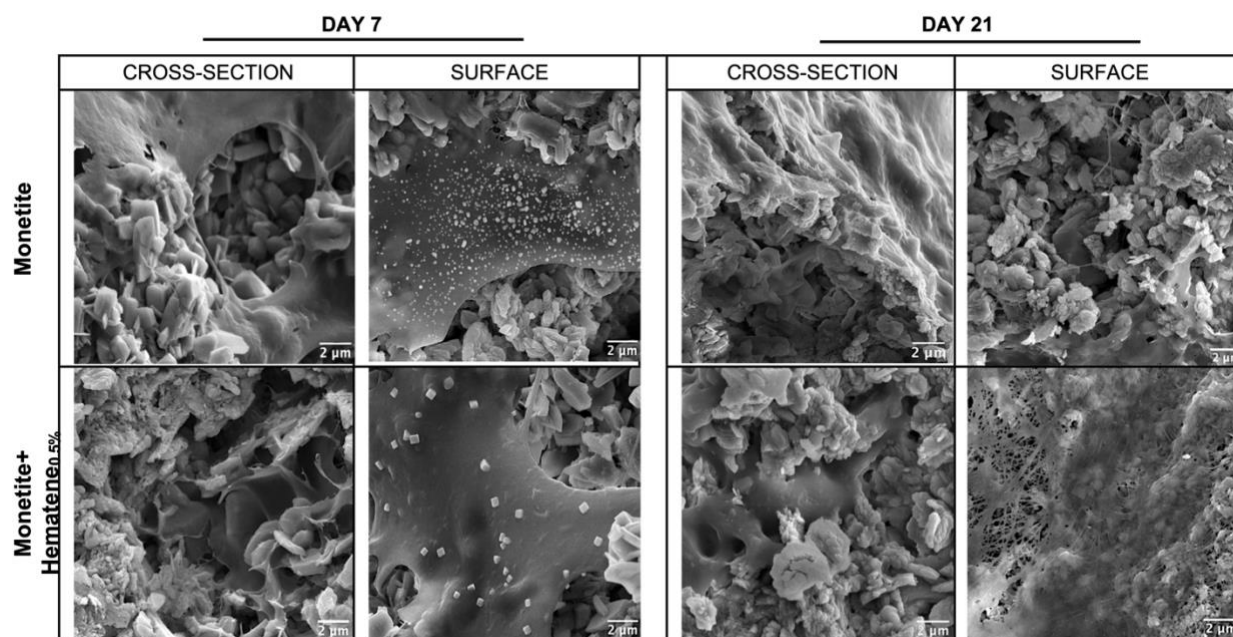


**Figure 4.9: Cross-sectional and surface views of cell-scaffold interactions.** SEM images of scaffolds before and after hematene loading at days 7 and 21 of culture. Both scaffold groups without cells (day 0) show the typical rectangular, plate-like morphology that is consistent with monetite. MC3T3-E1 cells after 7 and 21 days of culture exhibit good scaffold adhesion and morphological progression that is consistent with commitment to the osteogenic lineage.

### 4.2.4 Alkaline phosphatase (ALP) activity

Bioactive scaffolds can significantly influence cellular behavior and performance through ion release and surface properties. An early marker of osteogenic differentiation, ALP, was assessed to determine the osteogenic potency of hematene-treated scaffolds in OM. As presented in **Figure 4.10**, the ALP activity representative of osteoblastic activity was significantly

upregulated in the hematene-treated scaffolds at day 14. In fact, a 1.36- and 1.23-fold increase was shown relative to the untreated monetite and cell control, respectively. Though hematene-loaded scaffolds on day 7 displayed the highest ALP activity relative to all other conditions, no significant differences were detected. A uniform reduction in ALP activity appeared for all cultures at day 21 that signified the mineralization of the bone matrix. The ALP activity of MC3T3-E1 cells over 21 days *in vitro* demonstrated expressions that were consistent with normal osteoblast differentiation *in vivo*[172].

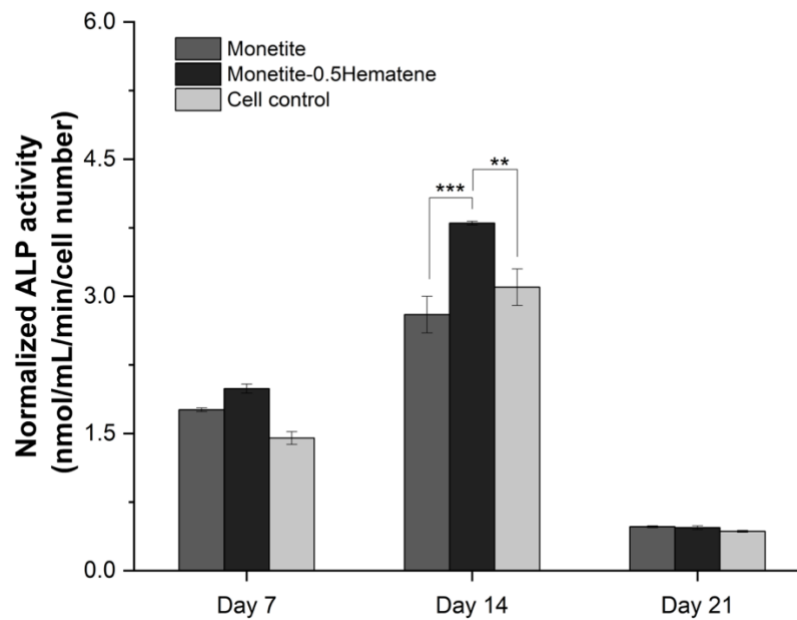


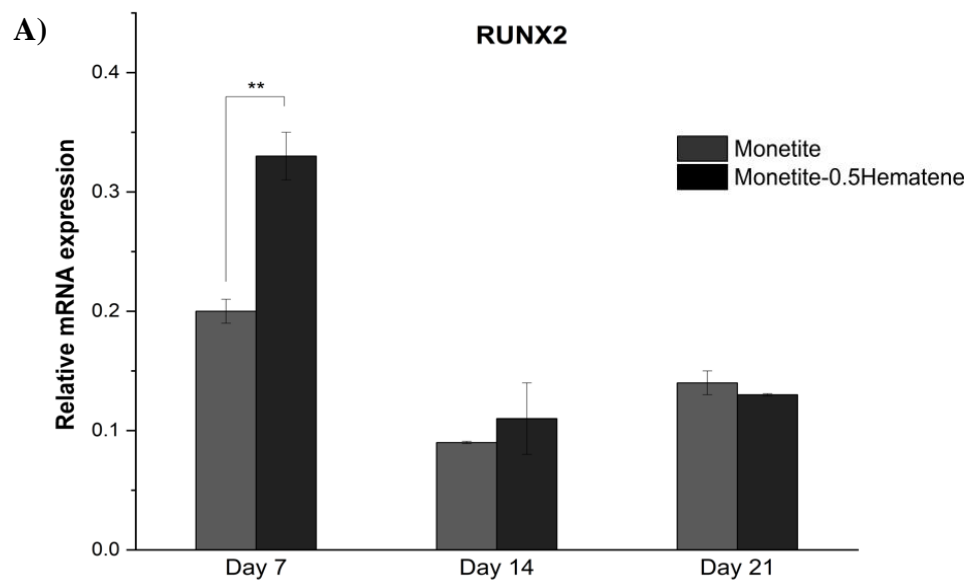
**Figure 4.10: ALP activity.** MC3T3-E1 cells cultured in 3D with untreated and treated scaffolds, and in 2D with monolayer controls for 21 days. ALP activity in serum for each condition was normalized to cell number and expressed as mean  $\pm$  standard deviation (n=3). Peak expressions of scaffolds on day 14 were corroborated by three independent experiments of triplicate observations.

#### 4.2.5 Real-time quantitative reverse transcription (RT-qPCR)

mRNA expressions of the Runx2 osteogenic-specific marker for all groups were maximally expressed at day 7 with a subsequent reduction at day 14, suggesting the transition from immature to mature osteoblasts during this period. At day 7, Runx2 expression was significantly upregulated in MC3T3-E1 cells cultured on hematene-treated scaffolds with a 1.6-fold increase relative to monetite controls (**Figure 4.11A**). Within and between group comparisons between days 7 and 14 revealed a 3.1- and 2.2- fold reduction in the treated and untreated monetite conditions, respectively. Though it was observed that the hematene-treated scaffolds still maintained a higher

expression of runx2 (relative 1.2-fold increase) at day 14, there was no significant difference detected between scaffold groups. The expression of runx2 was still present in both groups at similar levels at day 21.

Similarly, the expression of early bone-specific marker, Osteonectin (Sparc), showed to peak at day 7 in both groups coinciding with initial stages of differentiation. As presented in **Figure 4.11B**, osteonectin expression of cells cultured with hematene-treated scaffolds displayed an appreciable 1.36-fold increase at day 7 relative to monetite controls. By day 14, the level of osteonectin expression was significantly reduced confirming osteogenic differentiation of MC3T3-E1 cells with no significant difference observed between scaffold groups. While osteonectin expression in the hematene-treated scaffolds continued to decline further, an increased in osteonectin expression was observed from day 14 to day 21 in monetite control scaffolds that was significant within- and between-groups.



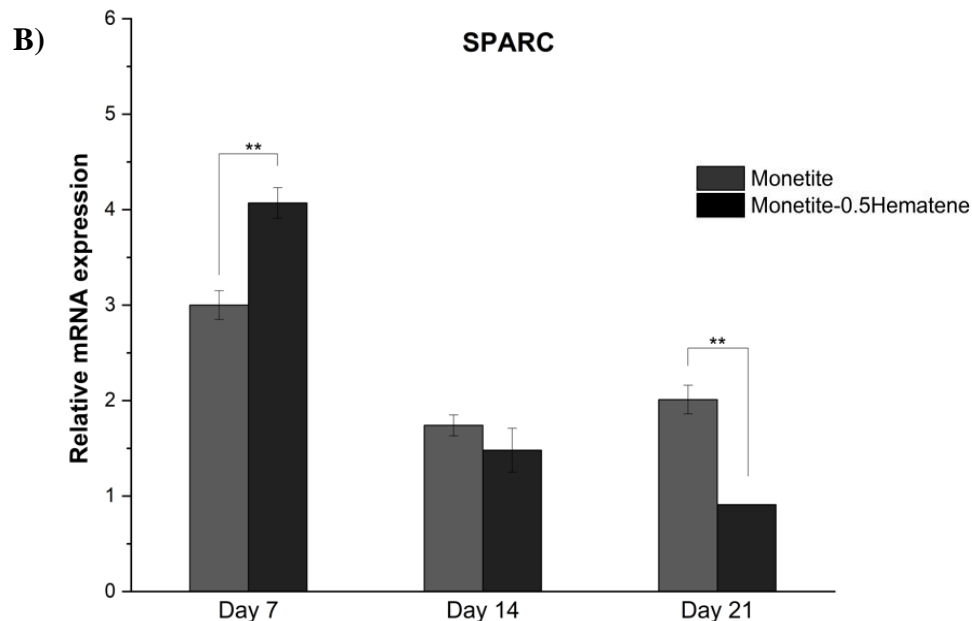


**Figure 4.11: RT-qPCR of osteogenic genes. A) Runx2**, master regulator of osteoblast differentiation **B) SPARC**, non-collagenous protein expressed in mineralized bone matrix. Data presented as relative mean  $\pm$  standard error.

## CHAPTER 5: DISCUSSION AND CONCLUSION

### 5.1 DISCUSSION

The direction towards improving the durability and biological activity of bioactive calcium phosphate scaffolds to be pursued for load-bearing applications. Modern nanomaterial lattices show significant opportunity to elevate the biological functionality and strength of scaffold systems. In this work, we sought to create a highly porous bioresorbable hematene-doped calcium phosphate scaffold with improved strength, functionality, and osteogenic potency for orthopaedic bone repair. Calcium phosphate cements were of significant interest given their compositional resemblance to native bone mineral. Specifically, bioactive and biodegradable monetite was selected based on its stability in physiological conditions and its incredible resorption. Of primary attention is 2D hematene, a graphene-like nanomaterial lattice that has rare 3D bonding networks and unique physiochemical properties that show the possibility of facilitating osteogenesis. It was

hypothesized that the bioactive potential of a hematene-doped implant would significantly improve bone formation.

We displayed the simplicity of obtaining ultrathin mono- and bilayer hematene nanosheets with a mean lateral size of 150nm with ultrasonic exfoliation from bulk hematite. To better improve the efficacy of exfoliation, bath sonication was combined with probe sonication to introduce highly localized shear forces for better material separation. Although hematene can be mechanically exfoliated using a high-speed amalgamator[173], this technique has low production yields and lacks the ability to control nanosheet thickness[174]. In this study, commonly used dimethylformamide (DMF) was replaced by another organic solvent, acetonitrile. Acetonitrile provided good dispersion of the hematene nanosheets while offering a lower boiling point for easier evaporation and better workability for *in vitro* experiments.

Most traditional orthopaedic materials provide insufficient biomimicry of the nanoscale topography and functionality of native bone that is required for ideal healing. For apatitic calcium phosphates, their success in bone repair applications is often limited by their low-negligible resorption rates[76]. In this study, hematene-treated and untreated monetite scaffolds exhibited gradual degradation profiles with a consistent weekly mass loss of 2.7% that was observed in parallel to monetite over 28 days of dynamic ageing. While both scaffold groups demonstrated a similar total mass loss of 10.5-10.9%, other studies using similar cement preparations have reported much lower values of 4.5% after 60 days of ageing in similar serum[81]. This may be due to the more aggressive dynamic ageing protocol that was implemented in this experiment to create better in-vivo like conditions.

Changes to scaffold architecture such as the predominant use of material coatings have been shown to influence biodegradation, mechanical performance, and biological responses[175, 176]. In this respect, a series of testing was performed to evaluate the effect of hematene loading on scaffold properties. Morphometrical analysis revealed that hematene-treated scaffolds exhibited a significant reduction in pore size, and while not significant, a 4% reduction in total porosity relative to monetite controls. These findings can be supported by the tendency of nanoparticle coatings and reinforcements to fill pore structures of a matrix, thereby reducing porosity and pore size, and ultimately increasing mechanical properties[177]. Despite these observable differences, both scaffold groups were in keeping with the reported average porosity for monetite (~45%)[178, 179], in addition to having pore sizes in the optimal range to support osteoblast activity (100-200

microns) [58]. In line with these structural trends is the significant improvement in compressive strength by 18% with just 0.5% hematene nanosheets relative to monetite controls.

The process of bone formation requires cell differentiation that happens in three stages: proliferation, maturation of the matrix, and mineralization. Particularly, cell proliferation before mineralization is reported to be a critical component to increase bone mass[180]. This can result from the release of calcium phosphate ions that activate bone cells to facilitate bone regeneration. However, material coatings are recognized as the first point of contact with the biological environment that can more closely define the fate of the biointerface based on the material's physicochemical properties. Our findings revealed that hematene-loaded scaffolds displayed good biocompatibility (>70%) and were able to significantly stimulate the proliferation of MC3T3-E1 cells. SEM images confirmed cell infiltration and migration in the interior and exterior parts of the scaffold with good cellular adhesion and morphological progression consistent with osteogenic commitment. At day 21, cells on the hematene-doped scaffolds were observed to almost cover the exterior of the scaffold. This difference in cell adhesion between the two scaffolds is likely from the promotion of protein adsorption by the hematene nanosheets at the biointerface, as demonstrated in previous studies with IONPS and graphene[181, 182].

ALP activity is a major regulator of bone mineralization and serves as a nonspecific marker of early bone formation and osteoblast activity. It was observed that ALP exhibited gradual increases in activity in until having achieved maximal peak expressions on day 14, with a subsequent reduction on day 21. ALP activity was found to be in accordance with the normal cell cycle for differentiation[172]. While hematene-loaded scaffolds exhibited significantly higher levels of ALP activity with peak expressions on day 14, this is inconsistent with the mRNA expression that was observed to be maximally expressed on day 7. Of note, this is not the first report that observed inconsistencies between gene expression and protein production[80, 183]. A transcriptional-level data analysis study has noted that protein and mRNA expression are not well correlated due to fundamental differences in translation, transcription, and half-lives/stability [184], and it is thought that protein turnover may influence the correlation between mRNA and protein abundance to a greater degree[185].

*Runx2* is the master gene of bone formation and a transcription marker of early osteoblast differentiation. *Runx2* is one of the most commonly studied biomarkers in bone development and repair with expressions coinciding with immature osteoblasts[186, 187]. Similarly, Osteonectin



(sparc) is a regulatory protein involved in early stromal mineralization (ie. initial differentiation) and osteoblastic growth that declines in mature osteoblasts similar to runx2[188]. Our findings showed that hematene-loaded scaffolds displayed a significantly greater level of runx2 and sparc expressions compared to untreated monetite. However, both scaffold groups demonstrated similar trends in peak expressions at day 7, with subsequent reduction at day 14 that was in accordance with early osteogenic differentiation. At day 21, runx2 was still present in both hematene-loaded and monetite scaffolds, suggesting that osteoblasts have not fully matured. While hematene-loaded scaffolds maintained low levels of osteonectin expression at days 14 and 21 that confirm osteogenic differentiation, monetite interestingly displayed an upregulated expression at day 21 that coincides with a delay in immature bone development. Further elucidation is required on the indifferences shown between mRNA and protein expressions. The investigation into late bone biomarker expressions is necessary to better understand the full osteogenic profiles of this novel construct.

The strong performance of monetite in bone repair compared to other CPCs is well acknowledged. However, monetite's full therapeutic potential in tissue engineering remains incompletely explored that has yet to be extensively studied with nano-driven strategies. Our findings suggest that hematene-loading can significantly enhance strength, functionality, and biological activity to drive bone repair. As this is the first report on hematene for orthopaedic bone repair, similar applications of graphene and its derivatives will be our main grounds for relative comparison. In a recent study with a 2D-based GO/La-monetite scaffold, GO showed to improve protein adsorption, proliferation, and osteogenic differentiation that was in accordance with our findings on hematene[189]. Interestingly, while we note a significant improvement from 0.5% hematene-loading onto monetite, it was shown here that compressive strength only increased by 1.10-fold with 3% GO reinforcement[189]. Other reports show similar findings in the ability of 2D materials to significantly influence bone repair using similar concentrations (0.5%), however, it is of note that GO was found to improve compressive strength by 3-fold in DCP cements which is far greater than the effect we observed with hematene[164].

## 5.2 CONCLUSION

In this work, the simplicity of obtaining ultrathin 2D hematene sheets through ultrasonic exfoliation was displayed, and their decoration over monetite implants without affecting crystallinity or thermal stability was observed. Hematene-doped monetite implants exhibited good biocompatibility that promoted cellular adhesion and stimulated enhanced cell proliferation of MC3T3-E1 cells. Reinforcement with hematene nanosheets demonstrated to significantly improve compressive strength of scaffolds by 18% compared to monetite alone. Excitingly, it was observed for the first time that hematene derivatives decorated over a monetite cement provided good surface functionalization for an osteoconductive matrix that enhanced the osteogenesis of MC3T3-E1 for bone repair. Together, these preliminary *in vitro* findings suggest that hematene derivative could be the next big candidate as a scaffold for bone tissue regeneration.

## 5.3 FUTURE WORKS

Future avenues to corroborate these findings can include exploring this potential within a stem cell model. Further insight into the relationship between nanosheet concentrations and osteogenesis would be of value, as well as exploring the osteoinductive ability of hematene derivatives. Furthermore, this novel 2D material offers encouraging avenues for advanced application by harnessing their unique magnetic and thermal properties as strategies to optimize bone repair.

## REFERENCES

1. Galindo-Moreno, P., et al., *Clinical and histologic comparison of two different composite grafts for sinus augmentation: a pilot clinical trial*. Clinical Oral Implants Research, 2008. **19**(8): p. 755-759.
2. Myeroff, C. and M. Archdeacon, *Autogenous bone graft: donor sites and techniques*. JBJS, 2011. **93**(23): p. 2227-2236.
3. O'Neill, C.N., Z.J. Walterscheid, and J.J. Carmouche, *A Novel Local Cancellous Autograft Source for Anterior Cervical Discectomy With Fusion*. Global Spine Journal, 2022. **12**(2): p. 190-197.
4. CARLISLE, E.R. and J.S. FISCHGRUND, *Bone graft and fusion enhancement*, in *Surgical Management of Spinal Deformities*. 2009, Elsevier. p. 433-448.
5. Bexkens, R., et al., *Donor-site morbidity after osteochondral autologous transplantation for osteochondritis dissecans of the capitellum: a systematic review and meta-analysis*. Knee Surgery, Sports Traumatology, Arthroscopy, 2017. **25**(7): p. 2237-2246.
6. Roberts, T.T. and A.J. Rosenbaum, *Bone grafts, bone substitutes and orthobiologics: the bridge between basic science and clinical advancements in fracture healing*. Organogenesis, 2012. **8**(4): p. 114-124.
7. Nather, A., A. Thambyah, and J. Goh, *Biomechanical strength of deep-frozen versus lyophilized large cortical allografts*. Clinical Biomechanics, 2004. **19**(5): p. 526-533.
8. Kennedy, R.H., C.R. Mills, and P. Brown, *Risk of infectious disease transmission through use of Allografts*, in *Oculoplastics and Orbit*. 2006, Springer. p. 3-18.
9. Engelman, G.H., et al., *Comparison of allograft versus autograft anterior cruciate ligament reconstruction graft survival in an active adolescent cohort*. The American journal of sports medicine, 2014. **42**(10): p. 2311-2318.
10. Friedlaender, G., *Appropriate screening for prevention of infection transmission by musculoskeletal allografts*. Instructional Course Lectures, 2000. **49**: p. 615-619.
11. Yildirim, M., et al., *Maxillary sinus augmentation using xenogenic bone substitute material Bio-Oss® in combination with venous blood: A histologic and histomorphometric study in humans*. Clinical oral implants research, 2000. **11**(3): p. 217-229.
12. Athanasiou, V.T., et al., *Histological comparison of autograft, allograft-DBM, xenograft, and synthetic grafts in a trabecular bone defect: an experimental study in rabbits*. Medical Science Monitor, 2009. **16**(1): p. BR24-BR31.
13. Galia, C.R., et al., *Physicochemical characterization of lyophilized bovine bone grafts*. Revista Brasileira de Ortopedia (English Edition), 2011. **46**(4): p. 444-451.
14. Offner, D., et al., *Bone grafts, bone substitutes and regenerative medicine acceptance for the management of bone defects among French population: issues about ethics, religion or fear?* Cell Medicine, 2019. **11**: p. 2155179019857661.
15. Stogov, M., D. Smolentsev, and E. Kireeva, *Bone Xenografts in Trauma and Orthopaedics (Analytical Review)*. Traumatology and Orthopedics of Russia, 2020. **26**(1): p. 181-189.

16. Schlickewei, W. and C. Schlickewei. *The use of bone substitutes in the treatment of bone defects—the clinical view and history*. in *Macromolecular symposia*. 2007. Wiley Online Library.
17. Hench, L.L. and I. Thompson, *Twenty-first century challenges for biomaterials*. Journal of the Royal Society Interface, 2010. **7**(suppl\_4): p. S379-S391.
18. Ødegaard, K.S., J. Torgersen, and C.W. Elverum, *Structural and biomedical properties of common additively manufactured biomaterials: A concise review*. Metals, 2020. **10**(12): p. 1677.
19. Ratner, B.D., et al., *Biomaterials science: an introduction to materials in medicine*. San Diego, California, 2004: p. 162-4.
20. Bergmann, F., et al., *Biomaterials Advances*.
21. Plenk Jr, H., *The role of materials biocompatibility for functional electrical stimulation applications*. Artificial organs, 2011. **35**(3): p. 237-241.
22. Ducheyne, P. and Q. Qiu, *Bioactive ceramics: the effect of surface reactivity on bone formation and bone cell function*. Biomaterials, 1999. **20**(23-24): p. 2287-2303.
23. Hench, L., *Bioglass and similar materials*. Encyclopedia of Materials: Science and Technology, 2001: p. 563-568.
24. Eppley, B.L. and A.M. Sadove, *A comparison of resorbable and metallic fixation in healing of calvarial bone grafts*. Plastic and reconstructive surgery, 1995. **96**(2): p. 316-322.
25. Amini, A.R., J.S. Wallace, and S.P. Nukavarapu, *Short-term and long-term effects of orthopedic biodegradable implants*. Journal of long-term effects of medical implants, 2011. **21**(2).
26. Veisheh, O. and A.J. Vegas, *Domesticating the foreign body response: recent advances and applications*. Advanced drug delivery reviews, 2019. **144**: p. 148-161.
27. Tsakiris, V., C. Tardei, and F.M. Clicinschi, *Biodegradable Mg alloys for orthopedic implants—a review*. Journal of Magnesium and Alloys, 2021.
28. Brydone, A., D. Meek, and S. Maclaine, *Bone grafting, orthopaedic biomaterials, and the clinical need for bone engineering*. Proceedings of the Institution of Mechanical Engineers, Part H: Journal of Engineering in Medicine, 2010. **224**(12): p. 1329-1343.
29. Li, J., et al., *Biophysical and biochemical cues of biomaterials guide mesenchymal stem cell behaviors*. Frontiers in Cell and Developmental Biology, 2021. **9**: p. 640388.
30. Chen, X., et al., *Scaffold structural microenvironmental cues to guide tissue regeneration in bone tissue applications*. Nanomaterials, 2018. **8**(11): p. 960.
31. Guvendiren, M., et al., *3D printed scaffold architecture controls stem cell differentiation*. Proc. Natl. Acad. Sci. USA, 2010. **107**: p. 4872-4877.
32. Fernandez-Yague, M.A., et al., *Biomimetic approaches in bone tissue engineering: Integrating biological and physicomechanical strategies*. Advanced drug delivery reviews, 2015. **84**: p. 1-29.
33. Huzum, B., et al., *Biocompatibility assessment of biomaterials used in orthopedic devices: An overview*. Experimental and Therapeutic Medicine, 2021. **22**(5): p. 1-9.
34. Babensee, J.E., et al., *Host response to tissue engineered devices*. Advanced drug delivery reviews, 1998. **33**(1-2): p. 111-139.

35. Pucino, V., et al., *Lactate buildup at the site of chronic inflammation promotes disease by inducing CD4+ T cell metabolic rewiring*. Cell metabolism, 2019. **30**(6): p. 1055-1074. e8.
36. Holloway, J.L., et al., *Modulating hydrogel crosslink density and degradation to control bone morphogenetic protein delivery and in vivo bone formation*. Journal of controlled release, 2014. **191**: p. 63-70.
37. Echeverria Molina, M.I., K.G. Malollari, and K. Komvopoulos, *Design challenges in polymeric scaffolds for tissue engineering*. Frontiers in Bioengineering and Biotechnology, 2021: p. 231.
38. Dhandayuthapani, B., et al., *Polymeric scaffolds in tissue engineering application: a review*. International journal of polymer science, 2011. **2011**.
39. Di Silvio, L. and P. Jayakumar, *Cellular response to osteoinductive materials in orthopaedic surgery*, in *Cellular Response to Biomaterials*. 2009, Elsevier. p. 313-343.
40. Foster, A.L., et al., *The influence of biomechanical stability on bone healing and fracture-related infection: the legacy of Stephan Perren*. Injury, 2021. **52**(1): p. 43-52.
41. Hak, D.J., et al., *The influence of fracture fixation biomechanics on fracture healing*. Orthopedics, 2010. **33**(10): p. 752-755.
42. Buckley, R. and C. Moran, *Apivatthakakul Th. AO principles of fracture management*. 2018, Thieme.
43. Miclau, T., et al., *Effects of delayed stabilization on fracture healing*. Journal of Orthopaedic Research, 2007. **25**(12): p. 1552-1558.
44. Ghiasi, M.S., et al., *Computational modeling of human bone fracture healing affected by different conditions of initial healing stage*. BMC musculoskeletal disorders, 2019. **20**(1): p. 1-14.
45. Weiner, S. and W. Traub, *Bone structure: from ångstroms to microns*. The FASEB journal, 1992. **6**(3): p. 879-885.
46. Gerhardt, L.-C. and A.R. Boccaccini, *Bioactive glass and glass-ceramic scaffolds for bone tissue engineering*. Materials, 2010. **3**(7): p. 3867-3910.
47. Fu, Q., et al., *Toward strong and tough glass and ceramic scaffolds for bone repair*. Advanced functional materials, 2013. **23**(44): p. 5461-5476.
48. Kutz, M., *Standard handbook of biomedical engineering & design*. 2003: McGraw-Hill Education.
49. Charrière, E., et al., *Mechanical characterization of brushite and hydroxyapatite cements*. Biomaterials, 2001. **22**(21): p. 2937-2945.
50. Urbanczyk, M., S.L. Layland, and K. Schenke-Layland, *The role of extracellular matrix in biomechanics and its impact on bioengineering of cells and 3D tissues*. Matrix Biology, 2020. **85**: p. 1-14.
51. Huo, Y., et al., *A critical review on the design, manufacturing and assessment of the bone scaffold for large bone defects*. Frontiers in Bioengineering and Biotechnology, 2021: p. 946.
52. Kim, K., et al., *Stereolithographic bone scaffold design parameters: osteogenic differentiation and signal expression*. Tissue Engineering Part B: Reviews, 2010. **16**(5): p. 523-539.

53. Rasouljanboroujeni, M., et al., *Dual porosity protein-based scaffolds with enhanced cell infiltration and proliferation*. Scientific reports, 2018. **8**(1): p. 1-10.
54. Turnbull, G., et al., *3D bioactive composite scaffolds for bone tissue engineering*. Bioactive materials, 2018. **3**(3): p. 278-314.
55. Karageorgiou, V. and D. Kaplan, *Porosity of 3D biomaterial scaffolds and osteogenesis*. Biomaterials, 2005. **26**(27): p. 5474-5491.
56. Martin, P., *Wound healing--aiming for perfect skin regeneration*. Science, 1997. **276**(5309): p. 75-81.
57. Sell, S., et al., *Scaffold permeability as a means to determine fiber diameter and pore size of electrospun fibrinogen*. Journal of Biomedical Materials Research Part A: An Official Journal of The Society for Biomaterials, The Japanese Society for Biomaterials, and The Australian Society for Biomaterials and the Korean Society for Biomaterials, 2008. **85**(1): p. 115-126.
58. Abbasi, N., et al., *Porous scaffolds for bone regeneration*. Journal of science: advanced materials and devices, 2020. **5**(1): p. 1-9.
59. Perez, R.A. and G. Mestres, *Role of pore size and morphology in musculo-skeletal tissue regeneration*. Materials Science and Engineering: C, 2016. **61**: p. 922-939.
60. Lossdörfer, S., et al., *Microrough implant surface topographies increase osteogenesis by reducing osteoclast formation and activity*. Journal of Biomedical Materials Research Part A: An Official Journal of The Society for Biomaterials, The Japanese Society for Biomaterials, and The Australian Society for Biomaterials and the Korean Society for Biomaterials, 2004. **70**(3): p. 361-369.
61. Yin, Z., et al., *The regulation of tendon stem cell differentiation by the alignment of nanofibers*. Biomaterials, 2010. **31**(8): p. 2163-2175.
62. Xin, Q., *Friction and lubrication in diesel engine system design*. 2013, Woodhead Publishing Sawston. p. 651-758.
63. Al-Omari, W., C. Mitchell, and J. Cunningham, *Surface roughness and wettability of enamel and dentine surfaces prepared with different dental burs*. Journal of Oral Rehabilitation, 2001. **28**(7): p. 645-650.
64. Ferrari, M., F. Cirisano, and M.C. Morán, *Mammalian cell behavior on hydrophobic substrates: influence of surface properties*. Colloids and Interfaces, 2019. **3**(2): p. 48.
65. Hill, G., *Benefits and associated risks of using allograft, autograft and synthetic bone fusion material for patients and service providers—a systematic review*. JBI Libr Syst Rev, 2010. **8**: p. 1-13.
66. Ishikawa, K., et al., *9.05 - Bioceramics*, in *Comprehensive Structural Integrity*, I. Milne, R.O. Ritchie, and B. Karihaloo, Editors. 2003, Pergamon: Oxford. p. 169-214.
67. Kucko, N.W., et al., *Chapter 34 - Calcium Phosphate Bioceramics and Cements*, in *Principles of Regenerative Medicine (Third Edition)*, A. Atala, et al., Editors. 2019, Academic Press: Boston. p. 591-611.
68. Bohner, M., et al., *Compositional changes of a dicalcium phosphate dihydrate cement after implantation in sheep*. Biomaterials, 2003. **24**(20): p. 3463-3474.

69. Wang, L., et al., *Effect of particle size on osteoinductive potential of microstructured biphasic calcium phosphate ceramic*. Journal of Biomedical Materials Research Part A, 2015. **103**(6): p. 1919-1929.
70. Tang, Z., et al., *The material and biological characteristics of osteoinductive calcium phosphate ceramics*. Regenerative biomaterials, 2018. **5**(1): p. 43-59.
71. Feng, X., *Chemical and biochemical basis of cell-bone matrix interaction in health and disease*. Current chemical biology, 2009. **3**(2): p. 189-196.
72. Kumar, R., et al., *Hydrogel-Nanofiber Composites for Tissue Reconstruction Applications: A State of the Art Review*. 2022.
73. Family, R., et al., *Surface modification for titanium implants by hydroxyapatite nanocomposite*. Caspian journal of internal medicine, 2012. **3**(3): p. 460.
74. Laasri, S., et al., *The affect of densification and dehydroxylation on the mechanical properties of stoichiometric hydroxyapatite bioceramics*. Materials Research Bulletin, 2010. **45**(10): p. 1433-1437.
75. Ruys, A., et al., *Sintering effects on the strength of hydroxyapatite*. Biomaterials, 1995. **16**(5): p. 409-415.
76. Bohner, M., *Calcium orthophosphates in medicine: from ceramics to calcium phosphate cements*. Injury, 2000. **31**: p. D37-D47.
77. Gbureck, U., et al., *Resorbable dicalcium phosphate bone substitutes prepared by 3D powder printing*. Advanced Functional Materials, 2007. **17**(18): p. 3940-3945.
78. Oryan, A., S. Alidadi, and A. Bigham-Sadegh, *Dicalcium phosphate anhydrous: an appropriate bioceramic in regeneration of critical-sized radial bone defects in rats*. Calcified tissue international, 2017. **101**(5): p. 530-544.
79. Habibovic, P., et al., *Osteoconduction and osteoinduction of low-temperature 3D printed bioceramic implants*. Biomaterials, 2008. **29**(7): p. 944-953.
80. Idowu, B., et al., *In vitro osteoinductive potential of porous monetite for bone tissue engineering*. Journal of tissue engineering, 2014. **5**: p. 2041731414536572.
81. Sheikh, Z., et al., *In vitro degradation and in vivo resorption of dicalcium phosphate cement based grafts*. Acta biomaterialia, 2015. **26**: p. 338-346.
82. Bohner, M., *Reactivity of calcium phosphate cements*. Journal of Materials Chemistry, 2007. **17**(38): p. 3980-3986.
83. Tamimi, F., Z. Sheikh, and J. Barralet, *Dicalcium phosphate cements: Brushite and monetite*. Acta biomaterialia, 2012. **8**(2): p. 474-487.
84. Bohner, M. and U. Gbureck, *Thermal reactions of brushite cements*. Journal of Biomedical Materials Research Part B: Applied Biomaterials: An Official Journal of The Society for Biomaterials, The Japanese Society for Biomaterials, and The Australian Society for Biomaterials and the Korean Society for Biomaterials, 2008. **84**(2): p. 375-385.
85. Barralet, J., L. Grover, and U. Gbureck, *Ionic modification of calcium phosphate cement viscosity. Part II: hypodermic injection and strength improvement of brushite cement*. Biomaterials, 2004. **25**(11): p. 2197-2203.
86. Alshaaer, M., et al., *Production of monetite-based Inorganic Phosphate Cement (M-IPC) using hydrothermal post curing (HTPC)*. Cement and Concrete Research, 2011. **41**(1): p. 30-37.

87. Tamimi, F., et al., *The effect of autoclaving on the physical and biological properties of dicalcium phosphate dihydrate bioceramics: brushite vs. monetite*. Acta Biomater, 2012. **8**(8): p. 3161-9.
88. Tamimi, F., et al., *Resorption of monetite granules in alveolar bone defects in human patients*. Biomaterials, 2010. **31**(10): p. 2762-2769.
89. Tamimi, F., et al., *The effect of autoclaving on the physical and biological properties of dicalcium phosphate dihydrate bioceramics: Brushite vs. monetite*. Acta biomaterialia, 2012. **8**(8): p. 3161-3169.
90. Tamimi, F., et al., *Resorption of monetite granules in alveolar bone defects in human patients*. Biomaterials, 2010. **31**(10): p. 2762-9.
91. Cama, G., *Calcium phosphate cements for bone regeneration*, in *Biomaterials for Bone Regeneration*. 2014, Elsevier. p. 3-25.
92. Lee, J.J., et al., *Dicalcium phosphate coated with graphene synergistically increases osteogenic differentiation in vitro*. Coatings, 2017. **8**(1): p. 13.
93. Berbezier, I. and M. De Crescenzi, *Self-assembly of nanostructures and nanomaterials*. 2015, Beilstein-Institut. p. 1397-1398.
94. Kumar, N. and S. Kumbhat, *Unique Properties, Essentials in nanoscience and nanotechnology*. 2016: John Wiley & Sons.
95. Trewyn, B.G., et al., *Synthesis and functionalization of a mesoporous silica nanoparticle based on the sol-gel process and applications in controlled release*. Accounts of chemical research, 2007. **40**(9): p. 846-853.
96. Arora, S., *Superparamagnetic iron oxide nanoparticles: magnetic nanoplatforms as drug carriers*. International journal of nanomedicine, 2012. **7**: p. 3445.
97. Bhattacharya, P.T., S.R. Misra, and M. Hussain, *Nutritional aspects of essential trace elements in oral health and disease: an extensive review*. Scientifica, 2016. **2016**.
98. Kambe, T., et al., *The physiological, biochemical, and molecular roles of zinc transporters in zinc homeostasis and metabolism*. Physiological reviews, 2015.
99. Bergman, B., *Concentration of zinc in some hard and soft tissues of rat determined by neutron activation analysis*. Acta Radiologica: Therapy, Physics, Biology, 1970. **9**(5): p. 420-432.
100. Iwata, M., et al., *Zinc accumulation and metallothionein gene expression in the proliferating epidermis during wound healing in mouse skin*. Histochemistry and Cell Biology, 1999. **112**(4): p. 283-290.
101. Calhoun, N. and J.C. Smith, *Uptake of <sup>65</sup>Zn in fractured bones*. Lancet, 1968. **2**.
102. Yamaguchi, M., H. Oishi, and Y. Suketa, *Stimulatory effect of zinc on bone formation in tissue culture*. Biochemical pharmacology, 1987. **36**(22): p. 4007-4012.
103. Hall, S., H. Dimai, and J. Farley, *Effects of zinc on human skeletal alkaline phosphatase activity in vitro*. Calcified Tissue International, 1999. **64**(2): p. 163-172.
104. Qiao, Y., et al., *Stimulation of bone growth following zinc incorporation into biomaterials*. Biomaterials, 2014. **35**(25): p. 6882-6897.
105. Program, T.P.H.A.o.C.C.N.I.S., *Device and surgical procedure-related infections in Canadian acute care hospitals from 2011 to 2020*. 2022(Volume 48-7/8, July/August 2022: Healthcare Associated Infections & Antimicrobial Resistance).



106. Kołodziejczak-Radzimska, A. and T. Jesionowski, *Zinc oxide—from synthesis to application: a review*. Materials, 2014. **7**(4): p. 2833-2881.
107. Li, Y., et al., *Zinc-doped hydroxyapatite and poly (propylene fumarate) nanocomposite scaffold for bone tissue engineering*. Journal of Materials Science, 2022. **57**(10): p. 5998-6012.
108. Katsumata, S.-i., et al., *Severe iron deficiency decreases both bone formation and bone resorption in rats*. The Journal of nutrition, 2009. **139**(2): p. 238-243.
109. Díaz-Castro, J., et al., *Severe nutritional iron-deficiency anaemia has a negative effect on some bone turnover biomarkers in rats*. European journal of nutrition, 2012. **51**(2): p. 241-247.
110. Medeiros, D.M., et al., *Iron deficiency negatively affects vertebrae and femurs of rats independently of energy intake and body weight*. The Journal of nutrition, 2004. **134**(11): p. 3061-3067.
111. Toxqui, L. and M.P. Vaquero, *Chronic iron deficiency as an emerging risk factor for osteoporosis: a hypothesis*. Nutrients, 2015. **7**(4): p. 2324-2344.
112. Ghaleb, A., et al., *Serum iron deficiency and 25-hydroxyvitamin D deficiency as an independent risk factor for osteoporosis in postmenopausal Arab women*. Journal of King Saud University-Science, 2021. **33**(1): p. 101217.
113. Bobo, D., et al., *Nanoparticle-based medicines: a review of FDA-approved materials and clinical trials to date*. Pharmaceutical research, 2016. **33**(10): p. 2373-2387.
114. Wang, Q., et al., *Response of MAPK pathway to iron oxide nanoparticles in vitro treatment promotes osteogenic differentiation of hBMSCs*. Biomaterials, 2016. **86**: p. 11-20.
115. Hu, S., et al., *Enhanced bone regeneration and visual monitoring via superparamagnetic iron oxide nanoparticle scaffold in rats*. Journal of Tissue Engineering and Regenerative Medicine, 2018. **12**(4): p. e2085-e2098.
116. Marycz, K., et al., *Iron oxides nanoparticles (IOs) exposed to magnetic field promote expression of osteogenic markers in osteoblasts through integrin alpha-3 (INTa-3) activation, inhibits osteoclasts activity and exerts anti-inflammatory action*. Journal of nanobiotechnology, 2020. **18**(1): p. 1-24.
117. Murthy, S., P. Effiong, and C.C. Fei, *Metal oxide nanoparticles in biomedical applications*, in *Metal Oxide Powder Technologies*. 2020, Elsevier. p. 233-251.
118. Vieira, D., et al., *Engineering surgical stitches to prevent bacterial infection*. Scientific reports, 2022. **12**(1): p. 1-11.
119. Seekaew, Y. and C. Wongchoosuk, *Introductory Chapter: 2D Materials*, in *2D Materials*. 2019, IntechOpen. p. 1.
120. Wang, J., G. Li, and L. Li, *Synthesis strategies about 2D materials*. Two-Dimensional Materials—Synthesis, Characterization and Potential Applications; Nayak, PK, Ed, 2016: p. 1-20.
121. Sui, X., et al., *2D material based advanced membranes for separations in organic solvents*. Small, 2020. **16**(50): p. 2003400.
122. Islam, M.A., et al., *Exfoliation mechanisms of 2D materials and their applications*. Applied Physics Reviews, 2022. **9**(4): p. 041301.

123. Furukawa, H., et al., *The chemistry and applications of metal-organic frameworks*. Science, 2013. **341**(6149): p. 1230444.
124. Kuila, T., et al., *Chemical functionalization of graphene and its applications*. Progress in Materials Science, 2012. **57**(7): p. 1061-1105.
125. Lee, C., et al., *Measurement of the elastic properties and intrinsic strength of monolayer graphene*. science, 2008. **321**(5887): p. 385-388.
126. Balandin, A.A., et al., *Superior thermal conductivity of single-layer graphene*. Nano letters, 2008. **8**(3): p. 902-907.
127. Du, X., et al., *Approaching ballistic transport in suspended graphene*. Nature nanotechnology, 2008. **3**(8): p. 491-495.
128. Dubey, N., et al., *Graphene: a versatile carbon-based material for bone tissue engineering*. Stem cells international, 2015. **2015**.
129. Lee, G.-H., et al., *High-strength chemical-vapor-deposited graphene and grain boundaries*. science, 2013. **340**(6136): p. 1073-1076.
130. Lin, J., Y. Huang, and P. Huang, *Graphene-based nanomaterials in bioimaging*. Biomedical Applications of Functionalized Nanomaterials, 2018: p. 247-287.
131. Liu, Z., et al., *PEGylated nanographene oxide for delivery of water-insoluble cancer drugs*. Journal of the American Chemical Society, 2008. **130**(33): p. 10876-10877.
132. Shadjou, N., M. Hasanzadeh, and B. Khalilzadeh, *Graphene based scaffolds on bone tissue engineering*. Bioengineered, 2018. **9**(1): p. 38-47.
133. Li, J., et al., *Electrical stimulation-induced osteogenesis of human adipose derived stem cells using a conductive graphene-cellulose scaffold*. Materials Science and Engineering: C, 2020. **107**: p. 110312.
134. Lakshmanan, R. and N. Maulik, *Graphene-based drug delivery systems in tissue engineering and nanomedicine*. Canadian journal of physiology and pharmacology, 2018. **96**(9): p. 869-878.
135. Iqbal, A.A., et al., *Graphene-based nanocomposites and their fabrication, mechanical properties and applications*. Materialia, 2020. **12**: p. 100815.
136. Malas, A., et al., *Effect of the GO reduction method on the dielectric properties, electrical conductivity and crystalline behavior of PEO/rGO nanocomposites*. Polymers, 2017. **9**(11): p. 613.
137. Baek, S.J., et al., *The effect of oxygen functional groups on the electrical transport behavior of a single piece multi-layered graphene oxide*. Synthetic metals, 2014. **191**: p. 1-5.
138. Zhang, S., et al., *Measuring the specific surface area of monolayer graphene oxide in water*. Materials Letters, 2020. **261**: p. 127098.
139. Ray, S.C., et al., *Graphene oxide (GO)/reduced-GO and their composite with conducting polymer nanostructure thin films for non-volatile memory device*. Microelectronic Engineering, 2015. **146**: p. 48-52.
140. Lu, G., L.E. Ocola, and J. Chen, *Reduced graphene oxide for room-temperature gas sensors*. Nanotechnology, 2009. **20**(44): p. 445502.
141. Menaa, F., A. Abdelghani, and B. Menaa, *Graphene nanomaterials as biocompatible and conductive scaffolds for stem cells: impact for tissue engineering and regenerative*

- medicine*. Journal of tissue engineering and regenerative medicine, 2015. **9**(12): p. 1321-1338.
142. Landi, G., et al., *Differences between graphene and graphene oxide in gelatin based systems for transient biodegradable energy storage applications*. Nanotechnology, 2016. **28**(5): p. 054005.
  143. Belaid, H., et al., *Development of new biocompatible 3D printed graphene oxide-based scaffolds*. Materials Science and Engineering: C, 2020. **110**: p. 110595.
  144. Saravanan, S., et al., *Scaffolds containing chitosan, gelatin and graphene oxide for bone tissue regeneration in vitro and in vivo*. International journal of biological macromolecules, 2017. **104**: p. 1975-1985.
  145. Li, J., et al., *Highly thermally conductive graphene film produced using glucose under low-temperature thermal annealing*. Journal of Materials Science, 2019. **54**(10): p. 7553-7562.
  146. Liu, S., et al., *Biocompatible graphene oxide–collagen composite aerogel for enhanced stiffness and in situ bone regeneration*. Materials Science and Engineering: C, 2019. **105**: p. 110137.
  147. Bahrami, S., N. Baheiraei, and M. Shahrezaee, *Biomimetic reduced graphene oxide coated collagen scaffold for in situ bone regeneration*. Scientific Reports, 2021. **11**(1): p. 1-10.
  148. Abazari, S., A. Shamsipur, and H.R. Bakhsheshi-Rad, *Reduced graphene oxide (RGO) reinforced Mg biocomposites for use as orthopedic applications: Mechanical properties, cytocompatibility and antibacterial activity*. Journal of Magnesium and Alloys, 2021.
  149. Yoon, O.J., et al., *Toxicity of graphene nanoflakes evaluated by cell-based electrochemical impedance biosensing*. Journal of Biomedical Materials Research Part A, 2014. **102**(7): p. 2288-2294.
  150. Wang, K., et al., *Biocompatibility of graphene oxide*. Nanoscale Res Lett, 2011. **6**(1): p. 1-8.
  151. Das, S., et al., *Oxygenated functional group density on graphene oxide: its effect on cell toxicity*. Particle & Particle Systems Characterization, 2013. **30**(2): p. 148-157.
  152. Zhang, Y., et al., *Cytotoxicity effects of graphene and single-wall carbon nanotubes in neural pheochromocytoma-derived PC12 cells*. ACS nano, 2010. **4**(6): p. 3181-3186.
  153. Puthirath Balan, A., et al., *Exfoliation of a non-van der Waals material from iron ore hematite*. Nature Nanotechnology, 2018. **13**(7): p. 602-609.
  154. Singla, R., et al., *Curie temperature engineering in a novel 2D analog of iron ore (hematene) via strain*. Nanoscale Advances, 2020. **2**(12): p. 5890-5896.
  155. Choudhuri, I., P. Bhauriyal, and B. Pathak, *Recent advances in graphene-like 2D materials for spintronics applications*. Chemistry of Materials, 2019. **31**(20): p. 8260-8285.
  156. Niu, T., J. Zhang, and W. Chen, *Surface Engineering of Two-Dimensional Materials*. ChemNanoMat, 2019. **5**(1): p. 6-23.
  157. Zhang, Z., et al., *Methanol electrooxidation with platinum decorated hematene Nanosheet*. Journal of The Electrochemical Society, 2019. **166**(4): p. H135.
  158. Xia, Y., et al., *Iron oxide nanoparticle-calcium phosphate cement enhanced the osteogenic activities of stem cells through WNT/ $\beta$ -catenin signaling*. Materials Science and Engineering: C, 2019. **104**: p. 109955.

159. Xia, Y., et al., *Novel magnetic calcium phosphate-stem cell construct with magnetic field enhances osteogenic differentiation and bone tissue engineering*. Materials Science and Engineering: C, 2019. **98**: p. 30-41.
160. Seonwoo, H., et al., *Reduced graphene oxide-incorporated calcium phosphate cements with pulsed electromagnetic fields for bone regeneration*. RSC advances, 2022. **12**(9): p. 5557-5570.
161. Lee, J.H., et al., *Enhanced osteogenesis by reduced graphene oxide/hydroxyapatite nanocomposites*. Scientific reports, 2015. **5**(1): p. 1-13.
162. Kim, J.-W., et al., *The effect of reduced graphene oxide-coated biphasic calcium phosphate bone graft material on osteogenesis*. International Journal of Molecular Sciences, 2017. **18**(8): p. 1725.
163. Pan, X., et al., *Iron-doped brushite bone cement scaffold with enhanced osteoconductivity and antimicrobial properties for jaw regeneration*. Ceramics International, 2021. **47**(18): p. 25810-25820.
164. Nasrollahi, N., et al., *Preparation of brushite cements with improved properties by adding graphene oxide*. International Journal of Nanomedicine, 2019. **14**: p. 3785.
165. Puthirath Balan, A., et al., *Exfoliation of a non-van der Waals material from iron ore hematite*. Nature Nanotechnology, 2018. **13**(7): p. 602-609.
166. Farshi Azhar, F., A. Olad, and R. Salehi, *Fabrication and characterization of chitosan–gelatin/nanohydroxyapatite–polyaniline composite with potential application in tissue engineering scaffolds*. Designed Monomers and Polymers, 2014. **17**(7): p. 654-667.
167. Nandagiri, V.K., et al., *Incorporation of PLGA nanoparticles into porous chitosan–gelatin scaffolds: Influence on the physical properties and cell behavior*. Journal of the mechanical behavior of biomedical materials, 2011. **4**(7): p. 1318-1327.
168. Grover, L., et al., *In vitro ageing of brushite calcium phosphate cement*. Biomaterials, 2003. **24**(23): p. 4133-4141.
169. Hsu, P.-Y., et al., *A head-to-head comparison of the degradation rate of resorbable bioceramics*. Materials Science and Engineering: C, 2020. **106**: p. 110175.
170. Chen, Y.-C., et al., *Long-term in vitro degradation and in vivo evaluation of resorbable bioceramics*. Journal of Materials Science: Materials in Medicine, 2021. **32**(1): p. 1-11.
171. Balan, A.P., et al., *Exfoliation of a non-van der Waals material from iron ore hematite*. Nature nanotechnology, 2018. **13**(7): p. 602-609.
172. Lian, J.B. and G.S. Stein, *Concepts of osteoblast growth and differentiation: basis for modulation of bone cell development and tissue formation*. Critical Reviews in Oral Biology & Medicine, 1992. **3**(3): p. 269-305.
173. Zhang, Z., et al., *2D hematene, a bioresorbable electrocatalytic support for glucose oxidation*. 2D Materials, 2020. **7**(2): p. 025044.
174. Liu, Y., X. Dong, and P. Chen, *Biological and chemical sensors based on graphene materials*. Chemical Society Reviews, 2012. **41**(6): p. 2283-2307.
175. Soares, L.E.S., et al., *Raman spectroscopy-multivariate analysis related to morphological surface features on nanomaterials applied for dentin coverage*. Spectrochimica Acta Part A: Molecular and Biomolecular Spectroscopy, 2020. **228**: p. 117818.

176. Böhner, M., et al., *Commentary: deciphering the link between architecture and biological response of a bone graft substitute*. Acta biomaterialia, 2011. **7**(2): p. 478-484.
177. Mokhtar, M., et al., *Mechanical performance, pore structure and micro-structural characteristics of graphene oxide nano platelets reinforced cement*. Construction and Building Materials, 2017. **138**: p. 333-339.
178. Cama, G., et al., *Structural changes and biological responsiveness of an injectable and mouldable monetite bone graft generated by a facile synthetic method*. Journal of the royal society interface, 2014. **11**(101): p. 20140727.
179. Cama, G., et al., *A novel method of forming micro-and macroporous monetite cements*. Journal of Materials Chemistry B, 2013. **1**(7): p. 958-969.
180. Hanna, H., L.M. Mir, and F.M. Andre, *In vitro osteoblastic differentiation of mesenchymal stem cells generates cell layers with distinct properties*. Stem cell research & therapy, 2018. **9**(1): p. 1-11.
181. Kumar, S. and S.H. Parekh, *Linking graphene-based material physicochemical properties with molecular adsorption, structure and cell fate*. Communications Chemistry, 2020. **3**(1): p. 1-11.
182. Zhu, Y., et al., *Dynamic protein corona influences immune-modulating osteogenesis in magnetic nanoparticle (MNP)-infiltrated bone regeneration scaffolds in vivo*. Nanoscale, 2019. **11**(14): p. 6817-6827.
183. Vogel, C., et al., *Sequence signatures and mRNA concentration can explain two-thirds of protein abundance variation in a human cell line*. Molecular systems biology, 2010. **6**(1): p. 400.
184. Mata, J., S. Marguerat, and J. Bähler, *Post-transcriptional control of gene expression: a genome-wide perspective*. Trends in biochemical sciences, 2005. **30**(9): p. 506-514.
185. Maier, T., M. Güell, and L. Serrano, *Correlation of mRNA and protein in complex biological samples*. FEBS letters, 2009. **583**(24): p. 3966-3973.
186. Maruyama, Z., et al., *Runx2 determines bone maturity and turnover rate in postnatal bone development and is involved in bone loss in estrogen deficiency*. Developmental dynamics: an official publication of the American Association of Anatomists, 2007. **236**(7): p. 1876-1890.
187. Qin, X., et al., *Runx2 regulates cranial suture closure by inducing hedgehog, Fgf, Wnt and Pthlh signaling pathway gene expressions in suture mesenchymal cells*. Human Molecular Genetics, 2019. **28**(6): p. 896-911.
188. Rosset, E.M. and A.D. Bradshaw, *SPARC/osteonectin in mineralized tissue*. Matrix Biology, 2016. **52**: p. 78-87.
189. Motameni, A., et al., *Graphene oxide reinforced doped dicalcium phosphate bone cements for bone tissue regenerations*. Journal of the Australian Ceramic Society, 2022: p. 1-15.

## APPENDICES

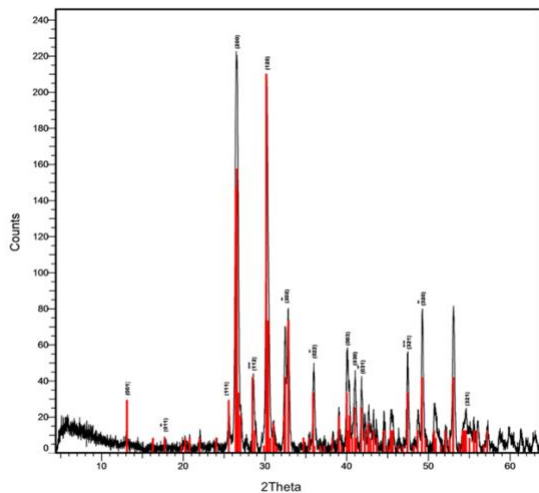


**Figure S1: XRD** Annotated miller indices of crystalline diffraction planes for monetite. Black and red spectra represent experimental and reference monetite, respectively.

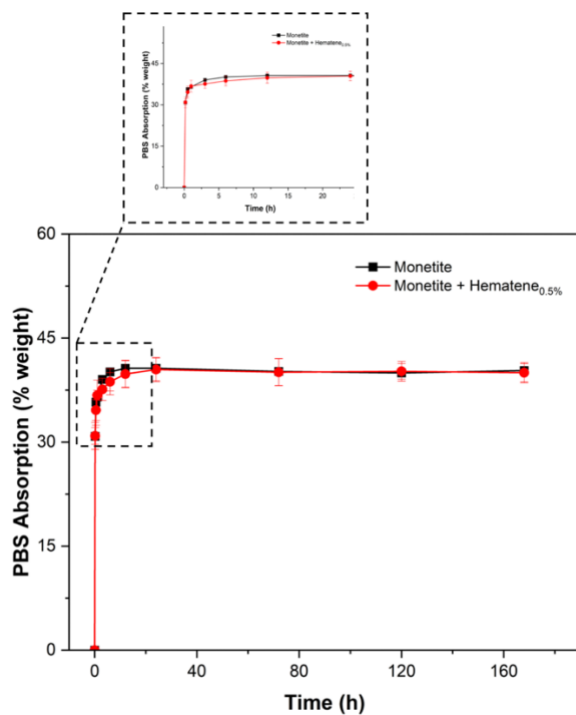


**Figure S2: Scaffold PBS Absorption.** Fluid absorption profiles of scaffolds left in vitro for 7 days. Hematene treated scaffolds show gradual fluid uptake with good stabilization in line with the untreated monetite controls. The absorption profiles appear ideal to facilitate cellular ingrowth, nutrient transport, and support mechanical integrity.

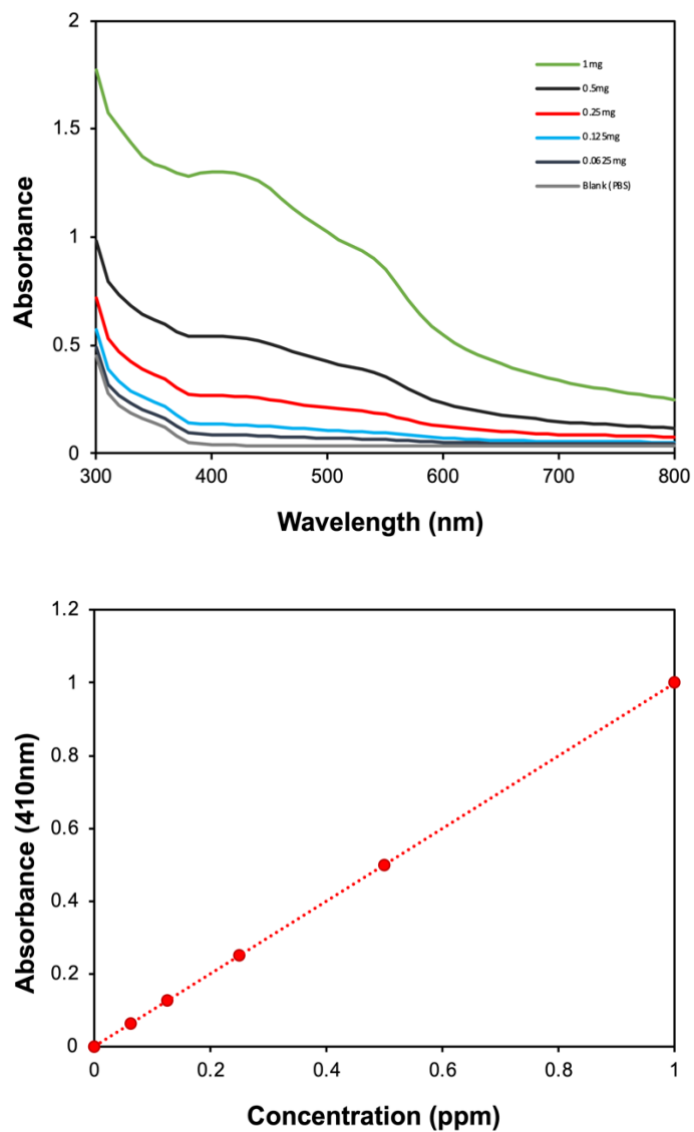


**Figure S3: Standard curve for hematene concentrations.** The determined wavelength of maximum absorbance ( $\lambda_{\text{max}}=410\text{nm}$ ) for hematene nanosheets. Standard curve showing Absorbance (410nm) vs Concentration (ppm) for known hematene concentrations 0.0625 to 1mg.

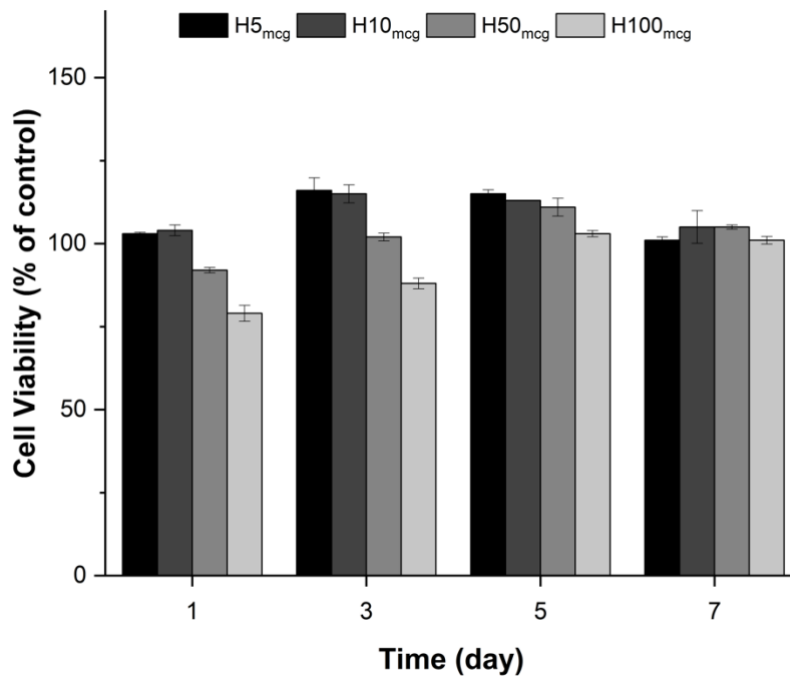


**Figure S4: Preliminary biocompatibility testing of hematene nanosheets.** Liquid suspensions of hematene nanosheets at 5, 10, 50, and 100mcg were cultured with MC3T3E1 cells in 2D (n=2) and normalized to untreated monolayers (100% viability). Cell viability expressed as mean percentage at days 1, 3, 5 and 7.

Hematene nanosheet suspensions with ranges from 5-100mcg was investigated for cytotoxic effects during preliminary testing prior to scaffold development. Testing confirmed good biocompatibility (>70%) of the standalone suspensions across all timepoints (**Figure S3**) that encouraged advancement to 3D systems. Though hematene nanosheets cultured at 100mcg were biocompatible, cell viability was found to be significantly diminished at days 1 and 3 relative to concentrations of 5 and 50mcg, and 5 and 10mcg, respectively. There were no significant differences detected between any conditions at day 5 and 7. Of all the concentrations, hematene nanosheet displayed the most biocompatibility with MC3T3-E1 cells when administered low concentrations of 5 to 10 mcg.